European Journal of Medicinal Chemistry 276 (2024) 116618

Contents lists available at ScienceDirect

European Journal of Medicinal Chemistry

journal homepage: www.elsevier.com/locate/ejmech

Research paper

Insights into the anticancer photodynamic activity of Ir(III) and Ru(II) polypyridyl complexes bearing β-carboline ligands

Juan Sanz-Villafruela [a,1], Cristina Bermejo-Casadesus [b,1], Elisenda Zafon [b,1], Marta Martínez-Alonso [a], Gema Durá [c], Aranzazu Heras [a], Iván Soriano-Díaz [d], Angelo Giussani [d], Enrique Ortí [d,**], Francesc Tebar [e,***], Gustavo Espino [a,****], Anna Massaguer [b,*]

[a] Universidad de Burgos, Departamento de Química, Facultad de Ciencias, Plaza Misael Bañuelos S/n, 09001, Burgos, Spain
[b] Universitat de Girona, Departament de Biologia, Facultat de Ciències, Maria Aurelia Capmany 40, 17003, Girona, Spain
[c] Universidad de Castilla-La Mancha, Departamento de Química Inorgánica, Orgánica y Bioquímica. Facultad de Químicas, Avda. Camilo J. Cela 10, 13071, Ciudad Real, Spain
[d] Instituto de Ciencia Molecular, Universidad de Valencia, Catedrático José Beltrán 2, 46980, Paterna, Spain
[e] Departament de Biomedicina, Unitat de Biologia Cel·lular, Facultat de Medicina i Ciències de la Salut, Centre de Recerca Biomèdica CELLEX, Institut d'Investigacions Biomèdiques August Pi i Sunyer (IDIBAPS), Universitat de Barcelona, 08036, Barcelona, Spain

ARTICLE INFO

Keywords:
Cancer
Photodynamic therapy
Cyclometalated complexes
Mitochondria

ABSTRACT

Ir(III) and Ru(II) polypyridyl complexes are promising photosensitizers (PSs) for photodynamic therapy (PDT) due to their outstanding photophysical properties. Herein, one series of cyclometallated Ir(III) complexes and two series of Ru(II) polypyridyl derivatives bearing three different thiazolyl-β-carboline NˆN′ ligands have been synthesized, aiming to evaluate the impact of the different metal fragments ($[Ir(C^N)_2]^+$ or $[Ru(N^N)_2]^{2+}$) and NˆN' ligands on the photophysical and biological properties. All the compounds exhibit remarkable photostability under blue-light irradiation and are emissive ($605 < \lambda_{em} < 720$ nm), with the Ru(II) derivatives displaying higher photoluminescence quantum yields and longer excited state lifetimes. The Ir PSs display pK_a values between 5.9 and 7.9, whereas their Ru counterparts are less acidic (p$K_a > 9.3$). The presence of the deprotonated form in the Ir-PSs favours the generation of reactive oxygen species (ROS) since, according to theoretical calculations, it features a low-lying ligand-centered triplet excited state ($T_1 = {}^3LC$) with a long lifetime. All compounds have demonstrated anticancer activity. Ir(III) complexes **1**–**3** exhibit the highest cytotoxicity in dark conditions, comparable to cisplatin. Their activity is notably enhanced by blue-light irradiation, resulting in nanomolar IC_{50} values and phototoxicity indexes (PIs) between 70 and 201 in different cancer cell lines. The Ir(III) PSs are also activated by green (with PI between 16 and 19.2) and red light in the case of complex **3** (PI = 8.5). Their antitumor efficacy is confirmed by clonogenic assays and using spheroid models. The Ir(III) complexes rapidly enter cells, accumulating in mitochondria and lysosomes. Upon photoactivation, they generate ROS, leading to mitochondrial dysfunction and lysosomal damage and ultimately cell apoptosis. Additionally, they inhibit cancer cell migration, a crucial step in metastasis. In contrast, Ru(II) complex **6** exhibits moderate mitochondrial activity. Overall, Ir(III) complexes **1**–**3** show potential for selective light-controlled cancer treatment, providing an alternative mechanism to chemotherapy and the ability to inhibit lethal cancer cell dissemination.

* Corresponding author.
** Corresponding author.
*** Corresponding author.
**** Corresponding author.
E-mail addresses: enrique.orti@uv.es (E. Ortí), tebar@ub.edu (F. Tebar), gespino@ubu.es (G. Espino), anna.massaguer@udg.edu (A. Massaguer).
[1] Equally contributed.

https://doi.org/10.1016/j.ejmech.2024.116618
Received 24 January 2024; Received in revised form 31 May 2024; Accepted 22 June 2024
Available online 28 June 2024

Abbreviations

2D	Two-dimensional
AO	Acridine orange
ATP	Adenosine triphosphate
ATCC	American type culture collection
BSA	Bovine serum albumin
CCCP	Carbonyl cyanide 3-chlorophenylhydrazone
CPCM	Conductor-like polarizable continuum model
CT	Charge transfer
DCF: 2′,7′	dichlorofluorescein
DCFDA 2′,7′	dichlorofluorescein diacetate
DFT	Density functional theory
DCM	Dichloromethane
DMEM	Dulbecco's modified Eagle's medium
DMSO	Dimethyl sulfoxide
EEA1	Early endosomal antigen 1
ECACC	European collection of authenticated cell cultures
EEs	Early endosomes
FBS	Fetal bovine serum
GFP	Green fluorescent protein
NMR	Nuclear magnetic resonance
HR-MS	High resolution mass spectrometry
IC_{50}	Half-maximal inhibitory concentration
ICP:MS	Inductively coupled plasma mass spectrometry
LC	Ligand centered
LBPA	Lysobisphosphatidic acid
LEs/Lys	Late endosomes/lysosomes
LLCT	Ligand-to-ligand charge transfer
MMP	Mitochondrial membrane potential
MLCT	Metal-to-ligand charge transfer
MTT	3-[4,5-dimethylthiazol-2-yl]-2,5 diphenyl tetrazolium bromide
NTOs	Natural transition orbitals
PBS	Phosphate buffered saline;
PEI	Polyethylenimine;
PES	Potential energy surface
PI	Phototoxicity index
PDT	Photodynamic therapy
PrI	Propidium Iodide;
PS	Photosensitizer
RBC	Red blood cells
ROS	Reactive oxygen species
SD	Standard deviation
TAP	1,4,5,8-tetraazaphenanthrene
Tom20	Translocase of the outer membrane subunit 20

1. Introduction

Chemotherapy is a fundamental component in the treatment of cancer, either used as a monotherapy or as an adjunct to surgery and radiotherapy. The discovery of cisplatin as an anticancer drug revealed the potential of metal-based complexes as chemotherapeutic agents. Today, platinum-based metal complexes such as cisplatin, oxaliplatin, and carboplatin are extensively used in clinical oncology [1]. However, some cancer types exhibit resistance to platinum-based treatments, and their efficacy in sensitive cancers is often restricted by side effects and the emergence of drug resistance [2]. Moreover, platinum compounds have limited effectiveness in treating metastasis, which accounts for over 90 % of cancer-related deaths [3]. Consequently, there is great interest in developing new chemotherapeutic agents with novel mechanisms of action aiming to reduce adverse effects, overcome multidrug resistance, and exhibit antimetastatic activity. In this regard, photodynamic therapy (PDT) with metal-based photosensitizers has emerged as a promising alternative. PDT is a clinically approved two-stage procedure that involves the administration of a photosensitizer (PS) followed by its controlled activation in the tumors by light irradiation. When photoactivated, the PS becomes electronically excited and displays photocatalytic activity in different types of reactions with cellular oxygen (O_2). This process leads to the generation of reactive oxygen species (ROS) that damage essential biomolecules and ultimately cause cancer cells death [4,5]. Moreover, PDT can activate an anti-cancer immune response [6]. The localized activation of PSs within tumors therefore enables selective targeting of cancer cells while minimizing damage to healthy tissues. Furthermore, since ROS act within a limited range of a few nanometers, it is possible to direct their activity towards specific subcellular organelles, such as mitochondria or lysosomes, through careful molecular design [7].

Ru(II) complexes of formula $[Ru(bpy)_2(N^{\wedge}N)]A_2$ (bpy = 2,2′-bipyridine, N^N = diimine ligands, A = counteranion) and Ir(III) biscyclometalated complexes of formula $[Ir(ppy)_2(N^{\wedge}N)]A$ (ppy = 2-phenylpyridinate) offer interesting possibilities for anticancer PDT. These compounds have common advantages such as easy preparation and modification due to the modular character of their synthesis, good cellular uptake and subcellular targeting capacity, photostability, phosphorescent properties for bioimaging with long emission lifetimes, one/two-photon excitation properties, and finally they also present excellent abilities to generate ROS in a photocatalytic manner [8]. These two families of metal complexes also show some differential properties. Thus, the dipositive Ru(II) derivatives tend to exhibit higher water solubility and wider absorption profiles in the visible region [9,10]. In contrast, the monopositive Ir(III) counterparts commonly display lower water solubility and inferior absorption in the visible region, but they offer excellent photoluminescent quantum yields, large Stokes shifts, and longer excited-state lifetimes due to the heavy-atom effect (large spin-orbit coupling constant of Ir) [11]. Indeed, polypyridine Ir(III) and Ru(II) metal complexes have demonstrated biological activity against various cellular organelles depending on their molecular structure. In particular, complexes fitted with a combination of cationic charge and lipophilicity exhibit preferential accumulation within mitochondria, due to the high membrane electric potential across the mitochondrial inner membrane, which is generated by the proton gradient during the electronic chain transport [12–15].

Mitochondria have emerged as appealing targets for cancer treatment due to their central role in cellular metabolism and bioenergetics, programmed cell death regulation, and redox balance [16]. Cancer cells depend to a high extend on mitochondrial metabolism to proliferate and survive, as it provides the major source of energy in form of ATP for tumour progression and supplies the metabolic intermediates for macromolecules biosynthesis. Furthermore, mitochondria are implicated in different steps of metastasis, including motility, invasion, plasticity, and colonization [17,18]. Different mitochondrial-targeted agents have shown promising results for cancer treatment when applied alone or in combination with other chemotherapeutic agents [19,20]. In cancer cells, the mitochondria exhibit varying degrees of dysfunction, such as increased mitochondrial membrane potential (MMP) and elevated production of ROS [21], which significantly increase their susceptibility to the photodynamic effects of cationic polypyridine metal complexes.

Lysosomes are also validated targets for anticancer therapy [22,23]. They are membrane-bound organelles characterized by a lumen with a pH ranging from 4.5 to 5, with hydrolytic enzymes functioning optimally at this acidic pH [24,25]. Lysosomes play a crucial role in intracellular digestion and recycling processes and are involved in the regulation of cellular homeostasis, apoptosis, and autophagy. There are increasing evidences that lysosomes also contribute to chemoresistance

by facilitating membrane trafficking of efflux transporters such as P-glycoprotein (P-gp), promoting drug sequestration, and modulating cell signalling [25]. Certain biscyclometalated Ir(III) complexes bearing β-carboline ligands exhibit a pH-responsive behaviour, which amplifies their activity in the acidic pH of lysosomes. In this environment, the aforementioned complexes have demonstrated increased photoluminescence and singlet oxygen generation upon light irradiation, as compared to neutral compartments [26,27]. Furthermore, it has been shown that a dual photocytotoxic effect at the level of both mitochondria and lysosomes notably enhances the antitumor effectiveness of agents active in PDT, since lysosomal dysfunction significantly compromises autophagy in response to cellular photodamage [28]. This cytoprotective mechanism enables cells to eliminate damaged proteins and organelles by their engulfment in double-membraned vesicles or autophagosomes, which subsequently fuse with lysosomes for degradation. In particular, clearance of oxidized or depolarized mitochondria (mitophagy) plays a crucial role in cell survival preventing the release of mitochondrial cytochrome *c*, activation of caspase 3, and induction of apoptosis [29,30].

With these ideas in mind and following our interest in developing new metal-based photosensitizers for anticancer PDT [12,31,32], we have synthesized three series of Ir(III) and Ru(II) cationic trischelate complexes bearing pH-sensitive β-carboline ligands ($[Ir(C^N)_2(N^N')]^+$ or $[Ru(N^N)_2(N^N')]^{2+}$) with the aim of studying their intracellular targeting properties and their potential as PDT photosensitizers. More specifically, we were interested in revealing the modulation ability of both the N^N' ligands (**L1**-**L3**) and the metal fragment, $[Ir(C^N)_2]^+$ or $[Ru(N^N)_2]^{2+}$, on the pK_a of our complexes and consequently on their photophysical properties and also on their intracellular distribution and photocytotoxicity, to establish the respective structure-activity relationships.

2. Material and methods

The synthetic procedures and the characterization data are shown in the supporting information.

2.1. Cell lines

The biological activity of the complexes was evaluated in five human cell lines. PC-3 prostate cancer, A549 basal lung adenocarcinoma, HeLa cervical carcinoma, and MCF-7 breast cancer cell lines were obtained from the American Type Culture Collection (ATCC). 1BR.3.G human skin fibroblasts were obtained from the European Collection of Authenticated Cell Cultures (ECACC). Cells were cultured in Dulbecco's modified Eagle's medium (DMEM) (Corning), supplemented with 10 % fetal bovine serum (FBS) (Gibco-BRL), 1 % L-glutamine (Corning), and 1 % penicillin-streptomycin (Corning) at 37 °C in a humidified atmosphere containing 5 % CO_2. Cells were maintained by successive trypsinization and seeding. The VenorH GeM Mycoplasma Detection Kit (Minerva Biolabs) was regularly used to check for potential mycoplasma contamination.

2.2. Cellular internalization

The cellular uptake of the compounds was assessed by flow cytometry using HeLa cells. Cells were seeded at a concentration of 100,000 cells/well in 12-well plates and incubated for 24 h. Subsequently, cells were treated with solutions of compounds **1**, **2**, and **3**, at 5 μM, which were freshly prepared by diluting aliquots of the corresponding 1 mM stock solution (see section 2.3) in cell culture medium, or medium alone as a control. Following incubation for different time intervals (1 min, 10 min, 30 min, 1 h, 2 h, 4 h, and 6 h), cells were washed with phosphate buffered saline (PBS) (Corning) and harvested by trypsinization. After washing with PBS, the fluorescence emission of 10,000 cells was measured at 675 nm using a Novocyte flow cytometer (Agilent Technologies) equipped with NovoExpress software. The median fluorescence of each sample was assessed relative to that of the untreated cells. To calculate the internalization kinetics, data were fitted to one-phase exponential association curves using GraphPad Prism software (GraphPad Software, Inc.). Three independent experiments were performed for each compound.

In addition, the internalization of the complexes was analyzed by determining the amount of metal present in the cells. To this end, HeLa cells were seeded in 6-well plates (Sarstedt) at a density of 2 million cells per well and allowed to attach overnight. Cells were then treated for 4 h with complexes **1**, **2**, **3**, and **6**, diluted from the 1 mM solutions in culture medium at 5 μM, or with medium alone as a control. After removing the treatments, cells were washed with PBS and harvested by trypsinization. The samples were then centrifuged and washed three more times with PBS. The number of cells in each sample was determined with the Novocyte flow cytometer. Subsequently, the amount of iridium or ruthenium in each sample was determined by inductively coupled plasma mass spectrometry (ICP-MS) analysis. Previously, cell pellets were dissolved in 400 μL of 69 % v:v nitric acid (PanReac Applichem) and heated at 100 °C for 18 h. After cooling, the samples were diluted with Milli-Q water to a final volume of 10 mL. The iridium or ruthenium content was quantified on an ICP-MS Agilent 7500c instrument at the Serveis Tècnics de Recerca, Universitat de Girona. The standards were freshly prepared in Milli-Q water with 2 % HNO3 before each experiment. The concentrations used for the calibration curve were 0, 1, 2, 5, 10 and 20 ppb. The isotopes detected were 193 Ir and 101 Ru. Readings were conducted in triplicate. Rhodium was added as an internal standard at a concentration of 10 ppb to all samples. Three independent replicates were performed for each complex. The amount of metal was expressed in relation to the number of cells (1 x 10^6) in each sample.

2.3. Cell viability assays

Cells were seeded on 96-well plates 24 h prior to the experiment at different concentrations depending on the cell line: 3000 PC-3 cells/well, 2500 A549 cells/well, 3500 MCF7 cells/well, 1500 HeLa cells/well or 5000 1BR.3.G cells/well. The compounds were diluted in sterile dimethyl sulfoxide (DMSO) and Milli-Q water to obtain 1 mM stock solutions (20 % DMSO v/v). To treat the cells, solutions ranging from 0 to 50 μM were prepared by diluting aliquots of the stock solutions in cell culture medium. This concentration range was expanded to 100 μM in cases where the IC_{50} values exceeded 50 μM. Cisplatin (1 mg/mL; Accord Healthcare) was used as a positive control. Cells were incubated with each solution for 6 h at 37 °C to allow the internalization of the compounds. Subsequently, the plates were kept in the dark or irradiated with a light-emitting diode (LED) system (LuxLight) for 1 h at different wavelengths (460 nm (blue), 515 nm (green), or 635 nm(red)), providing a total light dose of 24.1 J cm^{-2}. Each treatment was performed in triplicate. After 41 h, the treatments were removed, the cells were washed with PBS, and the cell viability was determined using the 3-[4,5-dimethylthiazol-2-yl]-2,5-diphenyltetrazolium bromide (MTT) assay. Cells were incubated for 2 h with 100 μL of fresh culture medium containing 10 μL of MTT solution (0.5 mg/mL) (Sigma-Aldrich). Then, the medium was discarded, and DMSO (Sigma-Aldrich) was added to each well to dissolve the purple formazan crystals. The absorbance of each well at a wavelength of 570 nm was determined using a Multiscan Plate Reader (Synergy 4, Biotek, Winooski, USA). For each compound, the concentration that inhibits cell viability by 50 % (IC_{50}) was determined using the Gen5 Data Analysis Software (BioTeck). Compounds with IC_{50} values greater than 100 μM were considered inactive. The phototoxicity index (PI=$IC_{50,dark}/IC_{50,light}$) was assessed for each compound. All experiments were performed at least in triplicate.

The cytotoxic activity of complex **1** was further evaluated against A549 cell spheroids. To generate the spheroids, cells were seeded at a density of 1500 cells per well into 96-well plates coated with a thin solidified layer of Geltrex™ reduced growth factor basement membrane matrix (Gibco) and left to grow in culture medium supplemented with 2 % Geltrex for 6 days. Then, spheroids were treated in the dark or under

blue light irradiation with dilutions of the complex ranging from 50 to 0.05 μM in cell culture medium containing 2 % Geltrex, as described above. Non-treated cells were used as control. After 41 h of incubation, the treatments were removed, cells were washed with PBS, and the % of viability was determined with CellTiter-Glo 3D reagent (Promega), following manufacturer's instructions. Briefly, 100 μL of complete medium and 100 μL of CellTiter-Glo 3D reagent were added to each well and then cells were kept in agitation for 5 min and incubated for 25 min at room temperature. The luminescence of each well was determined using a Multiscan Plate Reader (Synergy 4, Biotek, Winooski, USA) to assess the cell viability. Two independent experiments with duplicate samples were performed. The IC_{50} values were calculated with the Gen5 Data Analysis Software (BioTeck).

2.4. Clonogenic assays

PC-3 cells were seeded on 12-wells plates at a concentration of 100,000 cells/well. 24 h later, cells were incubated for 4h with solutions of complexes **1**, **2**, **3**, and **6** at the corresponding $IC_{50,light}$, which were freshly prepared by diluting the corresponding 1 mM stock solution in culture medium. Cisplatin (5 μM) was used as a positive control. The cells were subsequently kept in the dark or irradiated with blue light (460 nm) for 1 h. The treatments were then removed, and the cells were washed, trypsinized and counted. Three thousand cells were immediately plated in 5 cm diameter culture dishes and incubated for 10 days to allow the formation of colonies of at least 50 cells. The colonies were then fixed and stained with 1 % methylene blue in 70 % ethanol. Images of the plates were obtained using the Alpha Innotech Imaging System (Alpha Innotech). The number of colonies in each plate was determined using the Fiji ImageJ software [33]. Each compound was tested in triplicate.

2.5. Hemolysis assay

The hemolytic activity of the compounds was determined by measuring the hemoglobin release from red blood cells (RBD). Commercial porcine blood with sodium polyphosphate as an anticoagulant (Norfrisa, Spain), was diluted with PBS to a final concentration of 5 %. Aliquots of 150 μL were exposed to solutions of the complexes at the corresponding $IC_{50,light}$, which were freshly prepared by diluting the corresponding 1 mM stock solution in culture medium. Samples were incubated for 1 h at 37 °C in the dark or with blue light irradiation under constant agitation at 220 rpm in an orbital shaker. Treatment with Tween 0.2 % in PBS was used as the positive control to induce complete red blood cells (RBC) lysis. Subsequently, the samples were centrifuged to pellet the cells and 80 μL of supernatant was transferred to a 96-well plate and diluted with H_2O (80 μL). The absorbance of each well was measured with a Synergy 4 plate reader (Biotek) at 540 nm. The percentage of hemolysis H (%) was calculated with the formula: $H(\%) = 100 \times \frac{(Ax-An)}{(Ap-An)}$.

where Ax represents absorption of the sample, An represents absorption of the untreated negative control and Ap represents absorption of the positive control.

2.6. ROS measurement

Cellular ROS content was determined using the 5(6)-carboxy-2′,7′-dichlorofluorescein diacetate (Carboxy-DCFDA) (Sigma-Aldrich). HeLa cells were seeded on 12-well plates at a density of 100,000 cells/well. 24 h later, the cells were treated for 4 h at 37 °C with solutions of compounds **1**, **2**, **3**, and **6** at a dose corresponding to the $IC_{50,light}$, obtained by diluting the corresponding 1 mM stock solution in culture medium, or with medium alone as a control. After washing with PBS, cells were stained with 10 μM Carboxy-DCFDA for 30 min, washed again, and then photoactivated with blue light or incubated in the dark for 1 h. Cells were immediately collected by trypsinization and analyzed by flow cytometry using a Novocyte flow cytometer (Agilent Technologies) equipped with the NovoExpress software. The median fluorescence intensity of 10,000 cells was established, and the fold increase versus untreated control cells was determined. Three independent experiments were carried out for each compound.

2.7. Plasmids and transfection

HeLa cells were transfected with DNA using PEI (polyethylenimine) protocol. Cells were used for experiments 24 h after transfection. The Tom20(1–33)-GFP plasmid was obtained by subcloning DNA encoding Tom20 fragment corresponding to residues 1–33 into pEGFP-N1 (Clontech). The pEGFP-Rab5 and pEGFP-Rab7 vectors were kindly supplied by A. Sorkin (University of Pittsburgh, Pittsburgh, PA, USA). The GFP-CD63 construct was kindly supplied by J. Kluperman (University Medical Center Utrecht, Utrecht, Netherlands). Lamp2A, from Lamp2A-3xFlag, kindly provided by Mirka Allerding (Christian-Albrechts-Universität zu Kiel, Kiel, Germany), was subcloned into pEGFP plasmid (GFP-Lamp2A). MitoRed plasmid was acquired from Clontech.

2.8. Immunofluorescence staining

HeLa cells grown on coverslips were treated with complex **1** at 5 μM, prepared by diluting a 1 mM stock solution in cell culture medium, for time periods ranging from 30 to 45 min. After the treatment, cells were fixed with freshly prepared 4 % paraformaldehyde (Electron Microscopy Sciences) at room temperature for 15 min and mildly permeabilized with PBS containing 0.1 % Triton X-100 or 0.1 % saponin and 0.1 % bovine serum albumin (BSA) at room temperature for 5 min. After a 5 min incubation with blocking solution (PBS and 1 % BSA), the coverslips were incubated with the primary mouse anti-EEA1 (BD Biosciences) or anti-LBPA (clone6C4; Sigma-Aldrich) in PBS and 0.1 % BSA for 50 min at room temperature, washed intensively, and incubated with the appropriate secondary anti-bodies labeled with AlexaFluor-555 from Molecular Probes (Invitrogen-Life Technologies). After staining, the coverslips were mounted in Mowiol (Calbiochem). Complex **1** and TRITC images were acquired sequentially with 405 and 561 nm laser lines, an acoustic optical beam splitter, and emission detection ranges of 630–670 and 571–625 nm, respectively (TCS SP5 laser scanning confocal microscope; Leica Microsystems). Image processing was performed with ImageJ software (U.S. National Institutes of Health) [34].

2.9. Time-lapse microscopy

HeLa cells expressing the different fluorescent fusion proteins or transferrin conjugated with tetramethylrhodamine, or stained with the LysoTracker Red DND-99 or MitoTracker Green (M7514) dyes (Molecular Probes; Invitrogen-Life Technologies), were grown on 25 mm diameter glass coverslips (Warner Instruments) and mounted in an Attofluor chamber (Invitrogen-Life Technologies). Subsequently, cells were treated with complex **1** freshly prepared at 5 μM by diluting the 1 mM stock solution in cell culture medium. Time-lapse images were acquired every 1–2 min, up to a maximum of 30 min, using a Leica TCS SP5 laser-scanning confocal spectral microscope (Leica Microsystems) equipped with a DMI6000 inverted microscope and an incubation control system (37 °C, 5 % CO2). Complex **1**, GFP, and DsRed images were sequentially acquired with the 405, 488 and 561 nm laser lines and the emission detection ranges 630–670, 500–555 and 571–625 nm, respectively. Image processing was performed with ImageJ software. In vivo co-localization between complex **1** and mitochondria or endolysosomes compartments was analyzed from confocal images acquired after 30–60 min of the complex **1** incubation in cells expressing MitoRed or GFP-Rab7, respectively. Briefly, images were background substracted using FIJI-Image J software (Wayne Rasband, NIH) and the co-localization analysis performed with the plugin JACoP to determine the Pearson's Correlation Coefficient (PCC) in 20–25 cells per condition.

2.10. Determination of mitochondrial membrane potential

HeLa cells were seeded on 12-well plates at a concentration of 100,000 cells per well. After 24 h, the cells were incubated for 4 h with solutions of compounds **1**, **2**, **3**, and **6** at the corresponding $IC_{50,light}$, which were freshly prepared by diluting the corresponding 1 mM stock solution in culture medium. As a positive control, cells were co-incubated with carbonyl cyanide 3-chlorophenylhydrazone (CCCP) at 50 μM. Cells were then photoactivated with blue light or incubated in the dark for 1 h. Cells were immediately harvested by trypsinization and incubated with the JC-1 dye (Biotium) according to the manufacturer's instructions. The fluorescence of the cells was analyzed using a Novocyte flow cytometer. JC-1 was detected at 590 nm (FL2), to identify healthy mitochondria, and at 529 nm (FL1), to identify depolarized mitochondria. Each compound was tested in three independent experiments.

2.11. Evaluation of lysosomal damage

HeLa cells were seeded on glass-bottom chambered coverslips (μ-slide 8 well, Ibidi) at a concentration of 50,000 cells per well and allowed to attach for 24 h. Cells were then treated for 4 h with solutions of compounds **1**, **2**, **3**, and **6** at the corresponding $IC_{50,light,}$ obtained by diluting the corresponding 1 mM stock solution in culture medium, or with medium alone as a negative control. Cells were subsequently maintained in the dark or irradiated with blue light for 1 h. After removing the treatments, the cells were incubated with 5 μM of Acridine Orange (AO) (Sigma-Aldrich) at 37 °C for 15 min. Lysosomal damage was evaluated by confocal microscopy using a Nikon A1R confocal microscope. The cell cytoplasm and nucleoli were visualized in green (λ_{em} = 510 nm), while acidic cellular compartments such as lysosomes were visualized in red (λ_{em} = 625 nm). The images were analyzed using the NIS-Elements AR (Nikon, Japan) and Fiji/ImageJ software.

2.12. Apoptosis assay

The cell death pathway was analyzed with the Vybrant® Apoptosis Assay Kit (Molecular Probes). HeLa cells were seeded on 12-well plates at a concentration of 100,000 cells per well and treated under both dark and blue light conditions with solutions of compounds **1**, **2**, **3**, and **6** at the corresponding $IC_{50,light}$, prepared by diluting the corresponding 1 mM stock solution in culture medium, as previously described. Cisplatin was used as the positive control at a concentration of 50 μM. After 24 h of treatment, the cells were collected by trypsinization and stained with Annexin-V-FITC and propidium iodide according to the manufacturer's instructions. Samples were immediately analyzed using a Novocyte flow cytometer. Annexin-FITC staining was detected at a wavelength of 520 nm (FL1), and propidium iodide was detected at 617 nm (FL2). The fluorescence emission of 10,000 cells per sample was measured, and the percentage of live, early apoptotic, late apoptotic, and necrotic cell populations was determined. Three independent experiments were conducted.

2.13. Wound healing assay

A549 cells were selected for migration assays since they showed lower proliferation rate than HeLa cells. Cells were seeded at a density of 750,000 cells/well on 6 wells plates and allowed to attach for 24 h. Cells were incubated for 4 h with solutions of the compounds at the corresponding $IC_{50,light}$, which were prepared by diluting the corresponding 1 mM stock solution in culture medium. Samples were photoactivated or kept in the dark for 1 h. Cells were then washed twice with PBS, and a cross-shaped wound was made by scratching the confluent monolayer with a 200 μL pipette tip. Wells were washed again twice to remove the detached cells and incubated in incomplete media (DMEM supplemented with 0,5 % FBS, 1 % L-glutamine, and 1 % penicillin-streptomycin) for 24 h to avoid cell division. Untreated cells were used as control samples. Photographs of each side of the cross wound were obtained at 0, 16, and 24 h using an Olympus CKX41 Microscope equipped with the LCmicro software (Olympus). Analyses of cell migration were performed using the MRI Wound healing tool macro of Image J. Three independent experiments were performed for each compound.

2.14. Statistics

Statistical analysis was performed using *GraphPad Prism* (GraphPad Software). Quantitative variables were expressed as mean or median and standard deviation (SD). Statistical differences were analyzed by the Mann-Whitney non-parametric test. A value of $p < 0.05$ was considered statistically significant.

2.15. Computational details

All the triplet and singlet state minima of complexes **1—9** were optimized, without imposing any symmetry restriction, at the density functional theory (DFT) level of theory. Calculations were performed using the B3LYP exchange–correlation functional [35,36], which was previously employed to describe similar metal complexes [37,38]. The DEF2-SVP basis set [39–41] was selected for all the atoms in the complexes. The inner electrons for the Ir and Ru atoms were exchanged by the Stuttgart–Dresden effective core potential while explicitly treating the outer core electrons. Calculations involving triplet states were all carried out using the unrestricted approximation, checking that the spin contamination was between 1.95 and 2.05. Frequency calculations were executed to ensure the absence of imaginary frequencies within the optimized minima. This critical condition confirms the authenticity of the minima. To account for the influence of the surrounding solvent (H_2O), the conductor-like polarizable continuum model (CPCM) was employed [42]. All the calculations were performed with ORCA 5 software [43] and analyzed with the help of TheoDORE software [44]. To assign the nature of the different excited triplet states, time-dependent DFT (TD-DFT) calculations, at the same level of theory, were carried out as implemented in ORCA 5. To facilitate this assignment, natural transition orbitals (NTOs) [45] were obtained with TheoDORE software together to its fragment-based analysis.

Additional TD-DFT calculations were carried out to calculate the phosphorescence lifetimes (τ_{PL}) for the emitting triplet states at minimum-energy geometries obtained as described above. These calculations were performed using a SARC-ZORA-TZVP basis set [41,46] for Ir and Ru atoms and a ZORA-DEF2-SVP basis set [39] for all the other atoms, together with the ZORA Hamiltonian [47] to consider relativistic effects. In order to calculate τ_{PL} we followed the methodology employed in a previous work [38] for a similar family of iridium complexes.

3. Results and discussion

3.1. Synthesis of ligands and complexes

A total of nine complexes (**1**–**9**) were synthesized aiming to evaluate their potential use as photosensitizers in PDT. The synthesis of the ancillary N^N′ ligands **L1-L3** and the Ir(III) complexes **1**–**3** was already described in a previous study about their photocatalytic activity (Scheme 1) [48]. Herein, the synthesis of six new Ru(II) polypyridyl complexes of general formula *rac*-$[Ru(bpy)_2(N^N')](PF_6)_2$ (**4**–**6**) and *rac*-$[Ru(TAP)_2(N^N')](PF_6)_2$ (**7**–**9**), where bpy = 2,2′-bipyridine, TAP = 1,4,5,8-tetraazaphenanthrene and N^N' = **L1**-**L3**, is presented. Thus, we intend to assess the role of both the N^N′ ligands and the metal fragments ($[Ir(C^N)_2]^+$ and $[Ru(N^N)_2]^{2+}$) on the biological properties of the new photosensitizers. Indeed, the electron-deficient TAP ligand was chosen due to its potential to increase cellular photodamage [49].

The Ru(II) derivatives **4**–**9** were synthesized by heating *rac-cis*-$Ru(bpy)_2Cl_2$ or *rac-cis*-$Ru(TAP)_2Cl_2$ with the corresponding N^N' ligand, **L1-L3**, in a water:ethanol mixture (1:1; v/v) as shown in Scheme 2 [50].

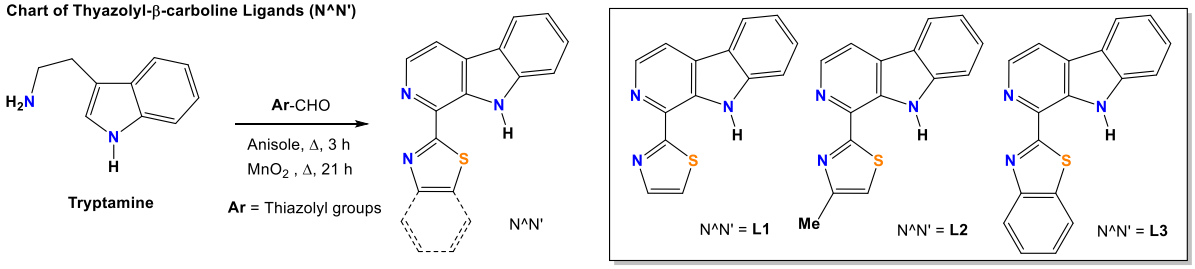

Scheme 1. Synthesis and molecular structure of the thiazolyl-β-carboline ligands **L1**-**L3**.

These reactions were carried out using a high pressure round bottom flask under a nitrogen atmosphere. The desired products were isolated as hexafluorophosphate salts in the form of racemic mixtures (Δ and Λ isomers) and are dark-red solids. All the complexes were isolated in good yields and purities according to analytical and spectroscopic data. TAP, *rac-cis*-Ru(bpy)$_2$Cl$_2$, and *rac-cis*-Ru(TAP)$_2$Cl$_2$ were prepared according to published procedures [51–53]. Analytical HPLC experiments confirmed the high purity of all PSs (>98 %, see Fig. S59).

3.2. Characterization of complexes

The identity and purity of the ligands and complexes were established by multinuclear nuclear magnetic resonance (NMR), high resolution mass spectrometry (HR-MS), and elemental analysis. The molecular structure of **2** and **3** was previously confirmed by X-ray diffraction [48]. In this work, the molecular structure of **5** and **6** was also confirmed by X-ray diffraction. The ^{1}H and ^{13}C{^{1}H} NMR spectra of Ir (III) and Ru(II) complexes were recorded in DMSO-d_6. The ^{1}H and ^{13}C {^{1}H} NMR spectra of Ru(II) complexes **4**–**9** confirmed the coordination of the ligand to the metal center and showed two sets of resonances for the bpy or TAP attributed to the asymmetry of these complexes. The HR-MS showed mass/charge ratios and isotopic distributions that corroborated the molecular structures proposed.

3.3. X-ray crystal structures

The crystal structures of *rac*-[Ru(bpy)$_2$(L2)](PF$_6$)$_2$·(H$_2$O) and *rac*-[Ru(bpy)$_2$(L3)](PF$_6$)$_2$·(H$_2$O)$_2$ were resolved by X-ray diffraction analysis. In both cases, high quality single crystals were obtained by slow evaporation from methanol solutions of **5** and **6**. Crystallographic refinement parameters are collected in Table S1. Selected bond distances and bond angles are given in Table 1. The unit cells of both crystal structures exhibit two pairs of the optical isomers (Λ and Δ), but Fig. 1 only shows the molecular structures of the respective Λ enantiomers. Two PF_6^- counterions and one or two water molecules per metal complex are also present in the unit cell. The molecular structure of these complexes shows the classical pseudo octahedral geometry with three N,N-donor ligands adopting bidentate chelate coordination modes. The Ru–N bond distances (2.051–2.101 Å) and coordination angles (78.1–79.53°) have standard values [50],54–56]. Nonetheless, the Ru–N distances for the β-carboline and thiazolyl entities are longer than those for the pyridine rings. The five-membered chelate rings of **L2** and **L3** in the coordination polyhedrons are essentially planar as shown by the respective torsion angles N–C–C–N (2.21 and 5.47°, respectively). Moreover, the crystal structure is held together mainly through hydrogen bonding interactions, involving the dicationic complexes as donors, the PF_6^- counterions as acceptors and the water molecules as both donors and acceptors

Table 1
Selected bond distances (Å) and angles (°) for compounds *rac*-[Ru(bpy)$_2$(L2)](PF$_6$)$_2$·(H$_2$O) (***rac*-5·(H$_2$O)**) and *rac*-[Ru(bpy)$_2$(L3)](PF$_6$)$_2$·(H$_2$O)$_2$ (***rac*-6·(H$_2$O)$_2$**).

Distances/angles	*rac*-5·(H$_2$O)	*rac*-6·(H$_2$O)$_2$
Ru(1)–N(1)	2.095(5)	2.092(4)
Ru(1)–N(2)	2.084(5)	2.101(4)
Ru(1)–N(4)	2.055(6)	2.056(4)
Ru(1)–N(5)	2.056(6)	2.051(4)
Ru(1)–N(6)	2.068(5)	2.071(4)
Ru(1)–N(7)	2.064(5)	2.067(4)
N(1)–Ru(1)–N(2)	78.1(2)	78.32(15)
N(4)–Ru(1)–N(5)	78.9(2)	79.53(17)
N(6)–Ru(1)–N(7)	78.8(2)	78.64(17)

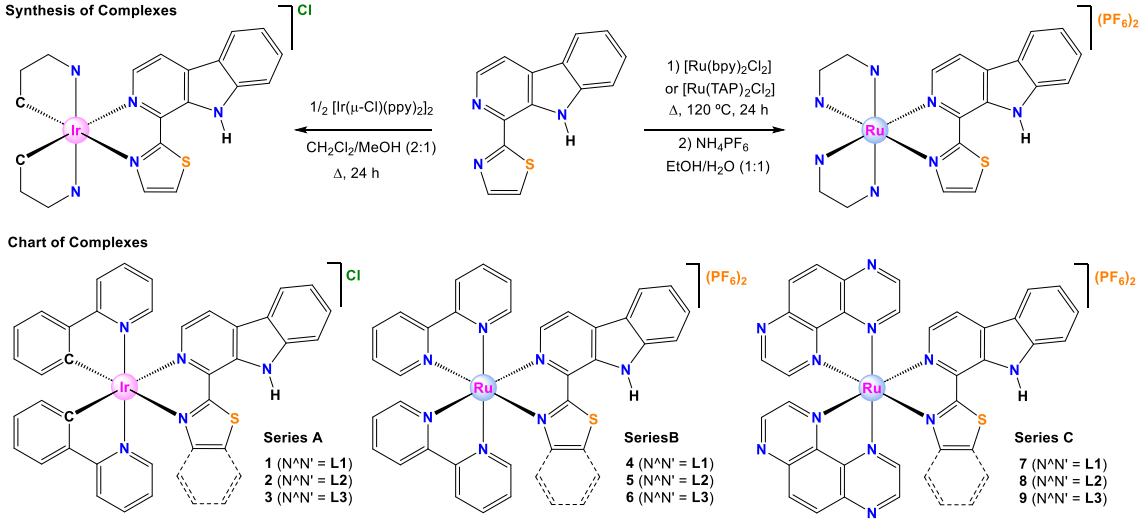

Scheme 2. Synthesis of complexes with **L1** as illustrative examples and molecular structure of complexes **1**–**9**.

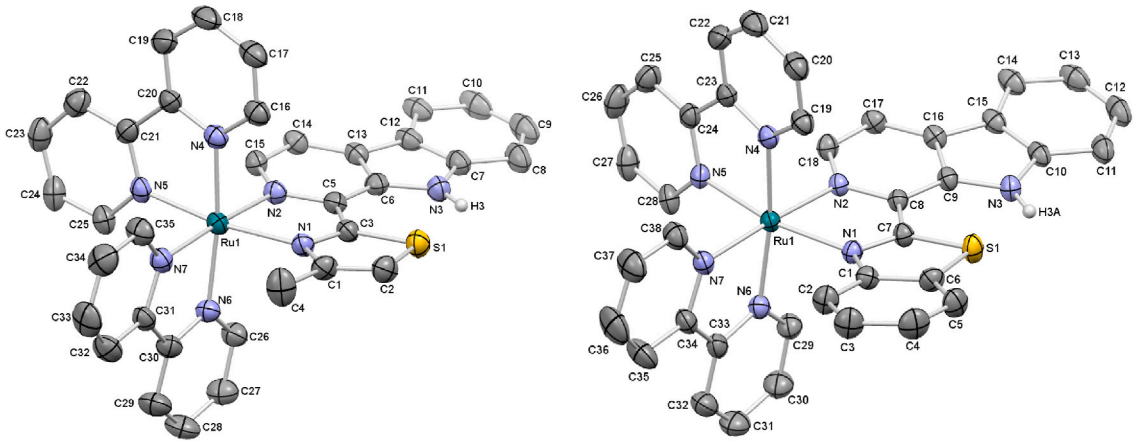

Fig. 1. ORTEP diagrams for the molecular structures of Λ-$[Ru(bpy)_2(L2)]^{2+}$ and Λ-$[Ru(bpy)_2(L3)]^{2+}$ in the crystal network of ***rac*-5·(H_2O)** and ***rac*-6·(H_2O)$_2$**. Thermal ellipsoids are shown at the 30 % probability level. Hydrogen atoms (except N–H), PF_6^- counterions, and water molecules are not shown for the sake of clarity.

(Table S2a and Fig. S31). However, double π,π-stacking contacts involving the β-carboline fragments are also observed (Table S2b and Fig. S31).

3.4. Photostability experiments

The photostability of aerated solutions (1.510^{-2}, or 5×10^{-3} M, DMSO-d_6:D_2O (3:2)) of our complexes was studied by ^{1}H NMR. The solutions were exposed to blue-light irradiation (λ_{irr} = 460 nm, 24 W) over a period of 24 h at room temperature. To our delight, no symptoms of photodegradation were observed, revealing that all the complexes exhibit an outstanding photostability, meaning that no structural alterations occur under these conditions (Figs. S32–S40).

3.5. Absorbance

The UV–Vis absorption spectra of the new complexes (10^{-5} M) were recorded at room temperature in both acetonitrile and in the mixture H_2O:DMSO (99:1). In both solvent systems, the absorption profiles are similar (Figs. S41–S42). The spectra of complexes **1**, **4**, and **7** in H_2O:DMSO are shown in Fig. 2 as representative examples. All the complexes exhibited strong bands with maxima between 240 and 290 nm that are attributed to spin-permitted ligand-centered transitions (^{1}LC, π → π*). In the 350–600 nm region, the Ir(III) complexes present an absorption band with maxima about 380 nm followed by a weak band that extends up to 550 nm. These bands are attributed to mixed spin-allowed and spin-forbidden metal-to-ligand charge transfer (^{1}MLCT and ^{3}MLCT) and ligand-to-ligand charge transfer (LLCT) transitions [57,58]. The absorption profile of complex **3** in water differs from that recorded in acetonitrile due to the presence of an absorption band centered at around 550 nm which spreads up to 650 nm (Figs. S41–42). This feature is attributed to the partial deprotonation of the N–H of the β-carboline ligand (*vide infra*) as predicted by theoretical calculations (Fig. S56). Complexes **4**, **5**, and **6** present two absorption bands centered at around 400 and 475 nm, respectively, and complexes **7**, **8**, and **9** display a main absorption band centered at around 420 nm. These bands are also attributed to ^{1}MLCT, ^{3}MLCT, and LLCT transitions.

3.6. Emission and photophysical properties

The emission spectra of **1**–**9** were recorded for both deoxygenated acetonitrile solutions (10^{-5} M) and aerated solutions in H_2O:DMSO mixtures (99:1) (10^{-5} M) at 25 °C. All the complexes exhibit a single broad emission band (Figs. S43–S44) and Stokes shifts larger than 192 nm (Table S3) in both solvent systems, which is consistent with

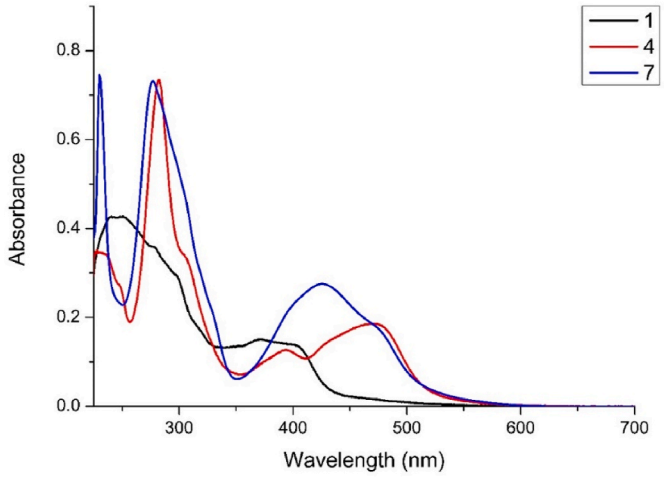

Fig. 2. Overlaid absorbance spectra of complexes **1**, **4**, and **7** in H_2O:DMSO (99:1, v:v) (10^{-5} M) at 25 °C.

phosphorescent emission. Fig. 3 shows the emission spectra of **1**, **4**, and **7** in H_2O:DMSO and Table 2 collects the photophysical data for all complexes in acetonitrile. These general features suggest a dominant charge-transfer (CT) character and a triplet nature for the emitting excited state [59]. The λ_{em} for some complexes is slightly red-shifted in H_2O:DMSO (99:1) compared to the respective λ_{em} in acetonitrile. Besides, the emission band of the Ru PSs is, in general, red-shifted with respect to the Ir analogues, except in the case of **9**. Regarding the effect of the N^N' ligand on the maximum emission wavelength, the experimental data indicate that **L2** causes a blue shift in λ_{em} for complexes **2**, **5**, and **8** in comparison to derivatives with **L1** (**1**, **4**, and **7**). In the case of **L3**, no clear trend can be established since a red shift is observed within the Ir series (λ_{em} = 648 nm for **1** vs λ_{em} = 678 nm for **3** in H_2O:DMSO, 99:1) and the Ru-bpy series (λ_{em} = 682 nm for **4** vs λ_{em} = 723 nm for **6** in H_2O:DMSO, 99:1), while an almost negligible blue shift is noticed for the Ru-TAP series (λ_{em} = 680 nm for **7** vs λ_{em} = 678 nm for **3** in H_2O:DMSO, 99:1).

The excited state lifetimes (τ) of **1**–**9** were determined in both deoxygenated CH_3CN and aerated H_2O:DMSO (99:1) solutions. In deoxygenated CH_3CN, all complexes showed moderate or long τ values (125–1525 ns) compatible with phosphorescent emission. In particular, complexes bearing ligand **L2** (**2**, **5**, and **8**) exhibit the longest τ values in each series, and complexes of the Ru-TAP series showed the highest τ values from 1090 to 1525 ns (Table 2). As expected, in aerated H_2O:

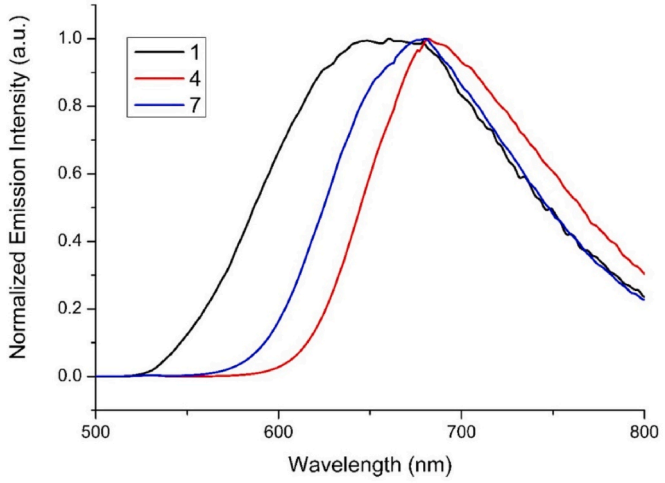

Fig. 3. Overlaid normalized emission spectra of complexes **1**, **4**, and **7** in H_2O:DMSO (99:1, v:v) (10^{-5} M) at 25 °C.

Table 2
Photophysical properties of complexes in acetonitrile (10^{-5} M) at 25 °C under a nitrogen atmosphere.

Complex	λ_{ex} (nm)	λ_{em} (nm)	τ (ns)	ϕ_{PL}(%)
1	405	641	125	2.08
2	405	605	**668**	1.83
3	405	652	183	0.54
4	450	679	679	16.40
5	450	677	**758**	**32.01**
6	450	720	284	7.46
7	450	650	1482	17.66
8	445	647	**1525**	**20.10**
9	450	642	1090	14.10

DMSO (99:1), the τ values are shorter for all the complexes due to the quenching effect attributed to O_2 (Table S3).

Regarding the photoluminescence quantum yields (ϕ_{PL}), the values recorded for the Ir(III) complexes in acetonitrile are very low (<2.1%). By contrast, the Ru(II) complexes exhibit higher ϕ_{PL} values (from 7.46 to 32.01%) and complexes **5** and **8** stand out with ϕ_{PL} values of 32.01 and 20.10%, respectively. The ϕ_{PL} in aerated H_2O:DMSO are low for all the complexes (Table S3).

3.7. Determination of pK_a

The complexes reported herein are expected to behave as weak acids due to the presence of a polar N–H bond in the β-carboline fragment. In particular, for the Ir(III) complexes under physiological conditions, the coordinated β-carboline ligands could undergo deprotonation of the N–H group to give either the neutral forms of the complexes or the equilibria between the cationic and neutral forms of the complexes depending on the pH. Indeed, the protonation state of the complexes could affect not only its global charge but also their solubility, aggregation state, and cellular uptake, as well as their absorption and emission profiles [60]. The pK_a values of Ir(III) complexes **1**, **2**, and **3** were experimentally determined by analyzing the variation of their emission intensity as a function of pH. As a matter of fact, the emission intensity of **1**, **2**, and **3** gradually decreases with increasing pH (Figs. S45–S47), as previously reported for similar derivatives [60–62]. The pK_a values determined experimentally were 7.9, 7.5, and 5.9 for **1**, **2**, and **3**, respectively. Therefore, we concluded that **2**, with a pK_a value very close to physiological pH (7.35–7.45), should be present in an equilibrium between its monocationic and neutral form, with a proportion close to 1:1. In the case of complex **1**, with a pKa value higher than physiological pH, the monocationic form is predominant, but it should coexists with the neutral form in a 3:1 ratio, approximately. In contrast, complex **3**, with a lower pK_a of 5.9, should adopt its neutral deprotonated form within most cellular organelles and its cationic protonated form in acidic organelles, such as lysosomes (Fig. S52). Indeed, **3** could be used to label lysosomes profiting from the expected pH-responsive emission enhancement at the acidic pH of these organelles. We interpret that the enhanced acidity of the N–H group in complex **3** is due to the higher conjugation provided by the extra benzene ring in **L3**, which stabilizes the negative formal charge of the ligand in the neutral form of **3** [63,64]. However, this is not the only factor ruling the acidity of this group (*vide infra*).

The pK_a values for selected Ru(II) complexes were determined by UV-VIS spectroscopy (Figs. 4 and 5 and Figs. S48–S51), since the variations of the emission intensity as a function of pH were not obvious for these compounds. The pK_a inferred for **4** and **6** (10.3 and 10.0, respectively) and for **7** and **9** (9.3 in both cases) were remarkably higher than those obtained for the corresponding Ir(III) counterparts, meaning that the Ru(II) complexes persist protonated in the cells. These results reveal that the $[Ir(ppy)_2]^+$ fragment increases the acidity of the N–H group more than the $[Ru(bpy)_2]^{2+}$ or $[Ru(TAP)_2]^{2+}$ fragments. Overall, the acidity of the N–H group depends on electronic effects stemming mainly from the metallic fragment, but also from the thiazolyl scaffold at some degree within the iridium derivatives.

3.8. Singlet oxygen quantum yields

Singlet oxygen quantum yields (Φ_Δ) were experimentally determined for representative complexes **1**, **4** and **7** using ABDA as a specific probe and Rose Bengal as the standard reference (Figs. S57–S58). The results obtained revealed that **1** is by far the most efficient photosensitizer (0.95) in good agreement with its high photo-induced cytotoxicity against cancer cells under light irradiation, while **4** and **7** provided lower φ_Δ values (0.25 and 0.61, see Table S8). A control experiment in the absence of PS was also performed to ruled out ABDA photobleaching.

3.9. Theoretical characterization

DFT-based electronic structure calculations on the Ir(III) and Ru(II) complexes **1**–**9** were performed in order to describe the photophysical properties of their lowest-energy triplet state (T_1 state), T_1 being strictly related to the capacity of a complex to act as photosensitizer. Since the key process of PDT is the transfer of energy from the T_1 state of the photosensitizer to molecular oxygen (which is the process resulting in

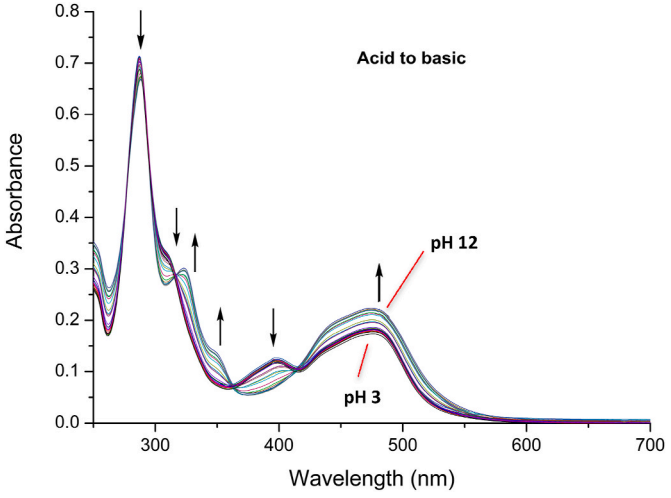

Fig. 4. Overlay of the absorbance spectra of **4** in H_2O:DMSO (99:1, v:v) (10^{-5} M) at 25 °C recorded at different pH values from 3 to 12.

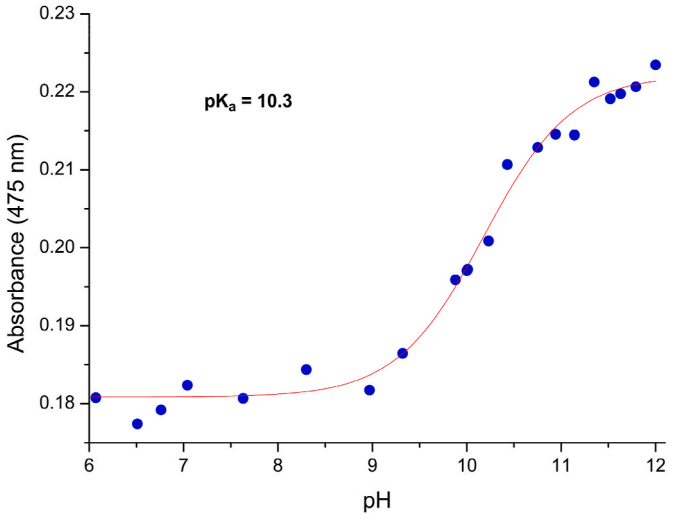

Fig. 5. Profile of the absorbance of **4** at 475 nm in H_2O:DMSO (99:1, v:v) (10^{-5} M) at 25 °C recorded as a function of pH between 6 and 12.

singlet-oxygen formation which in turn is responsible of cellular damage) it is essential to have a T_1 state that allows and promotes such an energy transfer. A prerequisite is that the T_1 state must have an energy greater than 1 eV (i.e., the T_1—S_0 energy difference computed at the T_1 minimum must be larger than 1 eV), because that is the energy required for promoting molecular oxygen from its triplet ground state to its reactive singlet excited state. Once such a condition is fulfilled, the longer the T_1 state lives without having the possibility to decay through radiative and/or non-radiative processes, the higher is the probability to interact with molecular oxygen and then produce singlet oxygen. The ideal case would then be a low emissive T_1 state, well separated from all other electronic states and in particular from the ground state, so that the excitation remains "trapped" in the T_1 minimum, "waiting for" the interaction with molecular oxygen. This reflects a situation in which the system takes a long time to emit (large phosphorescence lifetime) and at the same time has no accessible non-radiative decay path (high emission quantum yield). One of the most important non-radiative decay operating in Ir(III) and Ru(II) cationic complexes is related to the thermal population of triplet metal-centered (^{3}MC) states, which can easily cross with the ground state, then decaying along [37].

We then proceeded to the evaluation of radiative and non-radiative decays for the here studied complexes (see Fig. 6). Through the exploration of the T_1 potential energy surface (PES), a single T_1 minimum of ligand-to-ligand charge-transfer (^{3}LLCT) character was located for Ir(III) complexes except for complex **2**, which presents a ligand-centered (^{3}LC) nature. In contrast, three T_1 minima of metal-to-ligand CT (^{3}MLCT) and ^{3}LC nature were characterized for Ru(II) complexes (see Table S7 and Section 8 in the SI). LC states are in general considered to be slower emitters than CTs states, although such a vision has been recently revisited [38]. In order to evaluate the emission propensities, phosphorescence emission lifetimes were computed for all the T_1 minima. As shown in Table 3, Ru(II) complexes are predicted to have lifetime values one-to-three orders of magnitude larger than Ir(III) complexes. When considering only the lowest-energy T_1 minimum, the difference is reduced in most cases to one order of magnitude, however still reflecting a significantly slower emission process in Ru(II) complexes than in the Ir (III) analogues.

MC states were also characterized for the nine complexes. The adiabatic energy difference between each T_1 minimum and the lowest ^{3}MC minimum (hereafter $\Delta E_{T_1-{}^3MC}$) are also reported in Table 3. Such a value provides an estimation of how probable is to access from a T_1 minimum to the lowest non-emitting ^{3}MC state, and consequently determines the importance of non-radiative decays for each complex. As

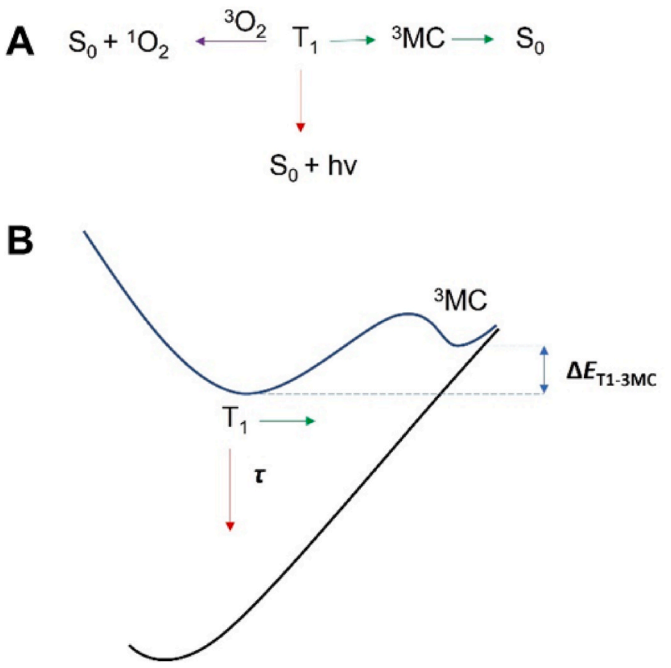

Fig. 6. A) Possible decay paths from the T_1 minimum. B) Representation of the radiative and non-radiative decay paths from the T_1 minimum along the PES, and the computed magnitudes (phosphorescence lifetime (τ) and adiabatic energy difference between T_1 and ^{3}MC ($\Delta E_{T_1-{}^3MC}$)) to estimate their relative importance.

shown in Table 3, Ru(II) complexes have very low $\Delta E_{T_1-{}^3MC}$ energy differences, much lower than those calculated for Ir(III) complexes, thus suggesting that the population of the non-emitting ^{3}MC states is more likely for the former. We then obtained that Ru(II) complexes have

Table 3
Vertical emission energies (E_{ver}, eV) from the optimized T_1 minima, adiabatic energy differences between each T_1 minimum and the ground state S_0 at its minimum (E_{adi}, eV), adiabatic energy differences between each T_1 minimum and the lowest MC minimum ($\Delta E_{T_1-{}^3MC}$, eV), and phosphorescence lifetimes (τ, μs) calculated for complexes **1**–**9**. The electronic nature of each T_1 minimum is also specified (see Table S7). "d" for **1**–**3** denotes the deprotonated structure of the complex.

Complex	State	E_{ver} (eV)	E_{adi} (eV)	$\Delta E_{T_1-{}^3MC}$ (eV)	τ (μs)
1	^{3}LLCT	1.92	2.16	0.69	1.33
1d	^{3}LC	1.57	1.74	1.16	155.27
2	^{3}LC	1.84	2.18	0.73	9.15
2d	^{3}LC	1.59	1.76	1.14	174.04
3	^{3}LLCT	1.85	2.08	0.61	1.65
3d	^{3}LC	1.52	1.69	1.22	247.47
4	^{3}MLCT$_1$	1.61	1.84	0.31	17.19
4	^{3}MLCT$_2$	1.80	2.04	0.11	153.31
4	^{3}MLCT$_3$	1.81	2.05	0.10	280.87
5	^{3}MLCT$_1$	1.64	1.87	0.20	16.43
5	^{3}MLCT$_2$	1.79	2.01	0.05	776.99
5	^{3}MLCT$_3$	1.81	2.04	0.02	1929.43
6	^{3}MLCT$_1$	1.50	1.73	0.31	24.52
6	^{3}MLCT$_2$	1.81	2.03	0.01	122.81
6	^{3}MLCT$_3$	1.83	2.06	−0.01	195.93
7	^{3}LC	1.81	2.10	0.02	78.69
7	^{3}MLCT$_1$	1.79	2.00	0.13	803.48
7	^{3}MLCT$_2$	1.79	2.00	0.12	747.92
8	^{3}LC	1.80	2.10	0.00	143.55
8	^{3}MLCT$_1$	1.77	1.97	0.13	479.71
8	^{3}MLCT$_2$	1.80	2.00	0.10	797.14
9	^{3}LC	1.70	2.01	0.07	80.71
9	^{3}MLCT$_1$	1.79	1.99	0.09	1253.97
9	^{3}MLCT$_2$	1.80	2.00	0.07	1361.32

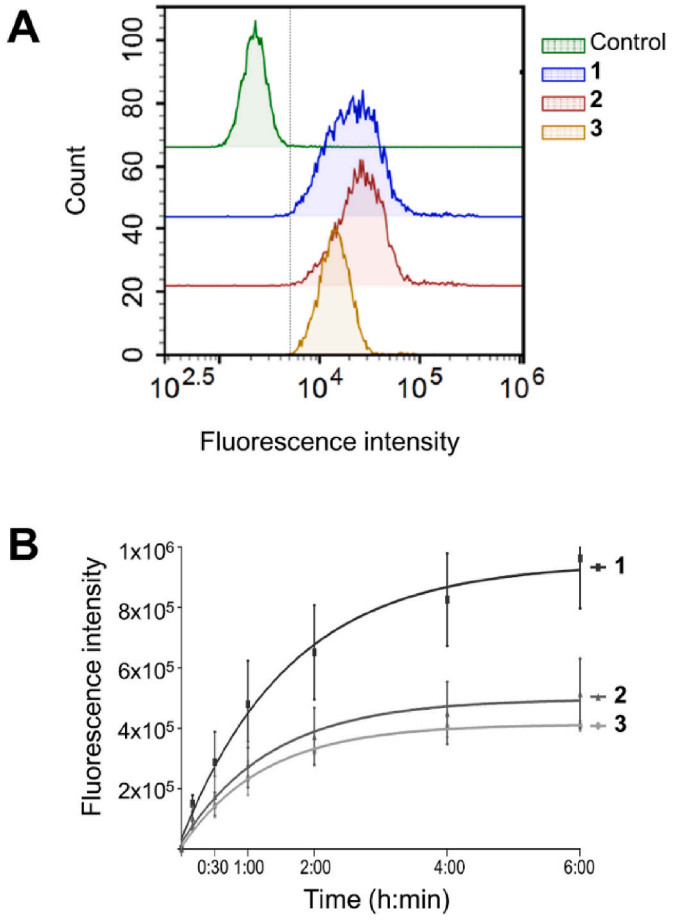

Fig. 7. A) Representative flow cytometry histograms showing the intracellular fluorescence of HeLa cells after 1 min of incubation with compounds **1**, **2**, and **3** at 5 μM. Untreated control cells were used as a reference. B) Cells were incubated for the indicated times with the compounds at 5 μM, and the median fluorescence intensity at each time point was determined by flow cytometry to assess the internalization kinetics. Data represents the mean ± SD of three independent experiments.

slower radiative processes but faster non-radiative decays, then precluding a direct explanation of the higher PI values characterizing Ir(III) complexes (*vide infra*).

An additional factor that needs consideration is the significantly lower pK_a values that characterize Ir(III) complexes compared to Ru(II) complexes (see Table S4). The pK_a values estimated for the three Ir(III) complexes suggest that both the protonated and deprotonated forms should be present at the physiological pH value of 7, in particular for complex **3** having a pK_a of 5.9. We then studied the photophysical properties of the three deprotonated Ir(III) complexes (hereafter named as **1d**, **2d**, and **3d**), and found a two-order of magnitude increase in the triplet state lifetimes, and an increase of $\Delta E_{T_1-{}^3MC}$ of around 0.5 eV (Table 3). The deprotonation actually causes a large stabilization of the LC state located on the ancillary ligand (*i.e.*, where the deprotonation takes place), which becomes the T_1 state, while leaving unaffected the MC state. So, the deprotonation globally determines an increase in the energy separation with the non-emitting MC states. In addition, the LC state of the deprotonated form resulted significantly lower emissive than the LLCT state of the protonated form, as reflected by the much higher triplet state lifetime calculated for the former (Table 3). Globally, the three deprotonated Ir(III) complexes display T_1 states that live longer, since both the radiative and non-radiative decays are slower in comparison with the protonated iridium complexes. This result can then rationalize the higher PI values (PI=$IC_{50,dark}/IC_{50,light}$) reported for the Ir(III) systems (*vide infra*, Table 4), and in particular the highest PI value obtained for complex **3**, for which the pK_a has the lowest value and a more significant presence of the deprotonated form is therefore expected.

Table 4
Phototoxicity of the complexes against PC-3 cancer cells.

Compound	IC_{50} (μM)		PI
	Dark	Light	
1	2.08 ± 0.48	0.021 ± 0.007	99.0
2	1.49 ± 0.38	0.017 ± 0.004	87.6
3	2.30 ± 0.86	0.017 ± 0.012	135.3
4	37.27 ± 18.89	2.65 ± 0.03	14.1
5	35.55 ± 3.40	2.20 ± 0.63	16.1
6	39.46 ± 6.60	3.32 ± 1.70	11.9
7	31.60 ± 2.13	6.77 ± 1.05	4.7
8	59.99 ± 13.63	8.48 ± 1.39	7.1
9	49.25 ± 20.90	2.97 ± 1.93	16.6
Cisplatin	2.53 ± 0.73	n.d.	–

PC-3 cells were treated with the compounds for 6 h at 37 °C to ensure their maximum internalization, and then kept in the dark or exposed to blue light for 1 h (460 nm, 24.1 J cm^{-2}). Cell viability was assessed 43 h later by MTT assays. Data represent the mean ± SD of at least three independent experiments, each performed in triplicate. n.d.: not determined. PI: phototoxicity index = $IC_{50,dark}/IC_{50,light}$.

3.10. Cellular uptake of the complexes

The efficient cellular uptake of the complexes is essential for their biological activity as photosensitizers. To assess cell internalization, the Ir(III) compounds **1**, **2**, and **3** were selected because of their demonstrated photoluminescence properties under cell culture conditions. Cells were incubated with the complexes at a concentration of 5 μM, and intracellular fluorescence was measured at various time points using flow cytometry. As shown in Fig. 7A, fluorescence emission from the complexes was detected in over 90 % of the cells after just 1 min of exposure. This rapid internalization suggests that the compounds enter the cells through diffusion across the cell membrane [65]. Moreover, since the fluorescence emission of complex **3** was dramatically suppressed at pH higher than 5.9, this finding suggests its rapid accumulation within acidic cellular compartments, such as lysosomes. Intracellular fluorescence was monitored for 6 h, and similar internalization kinetics were observed for the three compounds (Fig. 7B). Within the first 2 h, a linear increase in cellular fluorescence was observed, indicating a high uptake rate of the complexes during this period. After 2 h, the intracellular fluorescence levels began to stabilize, approaching saturation at 4 h. Based on these results, incubation times of at least 4 h were established to ensure maximum intracellular accumulation of the compounds before photoactivation, with the aim of achieving the most effective biological response.

3.11. Effect on cell viability

The anticancer activity of the complexes was evaluated against PC-3 cells in both dark and light-irradiation conditions. Cells were treated at concentrations ranging from 0.001 to 50 μM, and the concentration at which cell viability was inhibited by 50 % (IC_{50}) was determined for each compound. Compounds with IC_{50} values above 50 μM were further evaluated at a wider concentration range (up to 100 μM). The selection of the most promising candidates for PDT was based on the calculation of the phototoxicity index (PI=$IC_{50,dark}/IC_{50,light}$). As shown in Table 4, the three Ir(III) complexes exhibited notable antiproliferative effects in the dark, with $IC_{50,dark}$ values ranging from 1.49 to 2.30 μM, which are similar to the IC_{50} of the chemotherapeutic drug cisplatin under the same experimental conditions. In contrast, the Ru(II) complexes showed more moderate anticancer activity, with $IC_{50,dark}$ values between 35.55 and 39.46 μM for the complexes with bpy ligands and between 31.60

and 59.99 μM for complexes with TAP ligands. Importantly, upon irradiation with blue light, the activities of complexes **1**, **2**, and **3** were significantly increased, resulting in $IC_{50,light}$ values in the low nanomolar range and PI values of 99.0, 87.6, and 135.3, respectively. In contrast, despite their higher light absorption at 460 nm, the Ru(II) complexes exhibited $IC_{50,light}$ values ranging from 8.48 to 2.20 μM and markedly lower PI values (between 4.7 and 16.6).

The significant increase in the antiproliferative activity of the Ir(III) complexes after photoactivation highlighted their potential for PDT and prompted their selection for further investigation of their activity and their mechanism of action. The Ru (II) complex **6** was included in the study to examine the impact of the metallic fragment on the biological activity of these complexes.

The photocytotoxic behavior of **1**, **2**, **3**, and **6** was next investigated in response to irradiation with green (530 nm) and red (655 nm) light, as longer wavelengths have deeper tissue penetration capacities (Table 5) [66,67]. After irradiation with green light, PI values between 16 and 19.2 were obtained for the Ir(III) complexes, revealing a certain photoactivation capacity at 530 nm. Conversely, following irradiation with red light, the PI values of complexes **1** and **2** decreased significantly, which is consistent with the low light absorption observed for complex **1** at wavelengths above 550 nm (Fig. 2). In contrast, complex **3** exhibited a PI of 8.5. The deprotonated form of complex **3** presents one absorption band centered at 550 nm (Fig. S42) which spreads widely up to 650 nm and could explain its higher photoactivation by red light. In the case of the Ru(II) complex, an $IC_{50,light}$ value of 5.51 ± 1.76 μM was obtained upon irradiation with green light, resulting in a PI of 7.2. This value is slightly lower than the PI value obtained with blue light (11.9), indicating that complex **6** better maintains its photoactivation capacity under green light, which is consistent with its higher absorption at 530 nm (Fig. S42, Table 5).

The anticancer efficacy of complexes **1**, **2**, **3**, and **6** was further evaluated in human cancer cell lines of different origins: cervical (HeLa), lung (A549), and breast (MCF-7), as well as in non-malignant fibroblasts (1BR.3.G). As shown in Table 6, upon photoactivation with blue light, the $IC_{50,light}$ values for the three Ir(III) complexes remained in the low-nanomolar range in all cancer cell lines and PI values were between 70 and 201. The Ru(II) complex **6** also exhibited good phototoxicity in the different cell lines, with notable effectiveness against HeLa cells, although its activity was consistently lower than that of the structurally related Ir(III) complex **3**. It is worth noting that the IC_{50} values obtained against the 1BR.3.G fibroblast were, in general, slightly higher than those obtained in the cancer cell lines, especially for compounds **3** and **6**. Moreover, when comparing the cytotoxicity of the complexes towards fibroblast not exposed to the light and their activity against cancer cells upon irradiation, high photoselectivity indexes (PSI: $IC_{50,dark}$ in non-cancer cells/$IC_{50,light}$ in cancer cells) were observed. Specifically, a PSI of 543, 659, 461, and 769 were obtained for complex **3** in PC-3, HeLa, A549, and MCF7 cells, respectively. Therefore, the dose applied for photodynamic therapy (PDT) of these cancers would not have harmful effects on non-irradiated healthy tissues. In addition, it should be taken in consideration that PDT is being successfully applied to treat dermatological malignancies, which involve the local irradiation of the skin. Consequently, the light selectivity index (LSI = $IC_{50,light}$ skin fibroblasts/$IC_{50,light}$ cancer cells) was also calculated for all the complexes. Complex **3** was the only one that exhibited significant light selectivity in all tested cancer cell lines, with LSI values of 5.7, 6.9, 4.9, and 8.1, in PC-3, HeLa, A549, and MCF7 cells, respectively.

Table 5
Photocytotoxicity of complexes **1, 2, 3**, and **6** against PC-3 cancer cells upon photoactivation with green and red light.

Compound	Green Light		Red Light	
	IC_{50} (μM)	PI	IC_{50} (μM)	PI
1	0.13 ± 0.08	16	0.83 ± 0.20	2.5
2	0.085 ± 0.04	17.5	0.46 ± 0.05	3.2
3	0.12 ± 0.02	19.2	0.27 ± 0.08	8.5
6	5.51 ± 1.76	7.2	13.69 ± 0.34	2.9

PC-3 cells were incubated with the compounds for 6 h at 37 °C, then kept in the dark or exposed to green (530 nm) or red (655 nm) light for 1 h (24.1 J cm-2). Cell viability was assessed 41 h later by MTT assays. Data represent the mean ± SD of at least three independent experiments, each performed in triplicate. PI: phototoxicity index = $IC_{50,dark}/IC_{50,light}$.

3.12. Hemolytic activity

To further assess the potential toxicity of complexes **1**, **2**, **3,** and **6**, their activity against red blood cells (RBCs) was assessed. Complexes were incubated with RBCs freshly obtained from porcine blood at a concentration corresponding to their $IC_{50,light}$ in PC-3 cells (Table 4) and hemoglobin release was measured as an indicator of RBCs damage**.** None of the complexes displayed significant hemolytic activity, both in dark conditions and when exposed to blue light, as evidenced by hemolysis percentages below 2 % in all cases (Table S9). These results indicate the excellent blood compatibility of the complexes at the photocytotoxic concentrations. Furthermore, the absence of hemoglobin release from the RBCs indicates that the complexes do not cause direct damage to the cell membrane. This suggests that they interact with intracellular targets that are not present in RBCs, such as mitochondria or DNA.

3.13. Colony formation assays and effect on cell spheroids

The impact of the treatments on the long-term viability and growth potential of cancer cells was assessed using clonogenic assays. PC-3 cells were exposed to complexes **1**, **2**, **3**, and **6** at their respective $IC_{50,light}$ for 4 h, followed by either irradiation with blue light or incubation in the dark for 1 h. Cisplatin was used as a positive control. The treatments were removed, and the cells were seeded at low density and incubated to allow colony formation. As shown in Fig. 8A, the number of colonies was notably reduced by cisplatin and the photoactivated complexes. Specifically, in comparison to the untreated cells, the number of colonies was reduced to 14 ± 3 % after cisplatin treatment, and to 53 ± 2 %, 28 ± 3 %, 35 ± 2 %, and 56 ± 7 % after exposure to photoactivated complexes **1**, **2**, **3**, and **6**, respectively. However, none of the treatments in the dark induced any inhibition of colony formation (Fig. 8A and B). These findings confirm the photocytotoxicity of the complexes at their respective $IC_{50,light}$ and suggest that cell damage occurs during the photoactivation of the complexes. Hence, prolonged exposure to the compounds following photoactivation would not be necessary to inhibit cell proliferation.

Finally, the antitumor effect of complex **1** was tested using spheroids, which better mimic tumor biology than the two-dimensional (2D) cell cultures. Spheroids consist of microaggregates of cancer cells that recapitulate some important features of solid tumors, such as nutrient, growth factor, and oxygen gradients, as well as cell-cell and cell-extracellular matrix interactions [68,69]. Spheroids were generated from A549 cells, which were allowed to grow to form spherical aggregates ranging in size from 50 to 100 μm. The spheroids were subsequently treated with varying concentrations of complex **1** to determine its IC_{50} in this 3D model. Upon treatment under both dark and light conditions, a visible decrease in spheroid size was observed, albeit at different concentrations (Fig. 8C). Under dark conditions, an $IC_{50,dark}$ value of 11.95 ± 0.80 μM was obtained, which is approximately two times higher than the value obtained in the 2D cultures (Table 6). After irradiation, the $IC_{50,light}$ value was 0.36 ± 0.08 μM, resulting in a PI of 33.2. This value was 5.8 times higher than the $IC_{50,light}$ value obtained in 2D models, but was still within the nanomolar range, demonstrating the strong tumor growth inhibition capacity of the complex upon photoactivation.

Table 6
Photocytotoxicity of **1**, **2**, **3**, and **6** against HeLa, A549, and MCF7 cancer cells and 1BR.3.G fibroblasts.

Complex	HeLa			A549			MCF7			1BR.3.G		
	IC_{50} (μM)		PI	IC_{50} (μM)		PI	IC_{50} (μM)		PI	IC_{50} (μM)		PI
	Dark	Light		Dark	Light		Dark	Light		Dark	Light	
1	2.84 ± 0.90	0.018 ± 0.007	158	4.64 ± 3.25	0.062 ± 0.029	75	2.23 ± 0.47	0.025 ± 0.022	89	5.07 ± 0.83	0.056 ± 0.006	90
2	1.42 ± 0.72	0.016 ± 0.014	89	2.40 ± 1.56	0.035 ± 0.022	70	4.22 ± 0.28	0.021 ± 0.017	201	4.12 ± 0.78	0.032 ± 0.007	129
3	1.29 ± 0.34	0.014 ± 0.004	92	1.53 ± 0.24	0.02 ± 0.005	76	1.32 ± 0.40	0.012 ± 0.002	110	9.23 ± 0.46	0.097 ± 0.010	95
6	56.62 ± 5.68	1.32 ± 0.24	43	35.12 ± 11.47	1.83 ± 1.32	19	28.27 ± 6.51	1.37 ± 0.52	21	92.81 ± 5.82	3.68 ± 0.27	25

HeLa, A549, MCF7 and 1BR.3.G cells were incubated with the compounds for 6 h at 37 °C, then kept in the dark or exposed to blue light for 1 h (460 nm, 24.1 J cm^{-2}). Cell viability was assessed 41 h later by MTT assays. Data represent the mean ± SD of at least three independent experiments, each performed in triplicate. PI: phototoxicity index = $IC_{50,dark}/IC_{50,light}$.

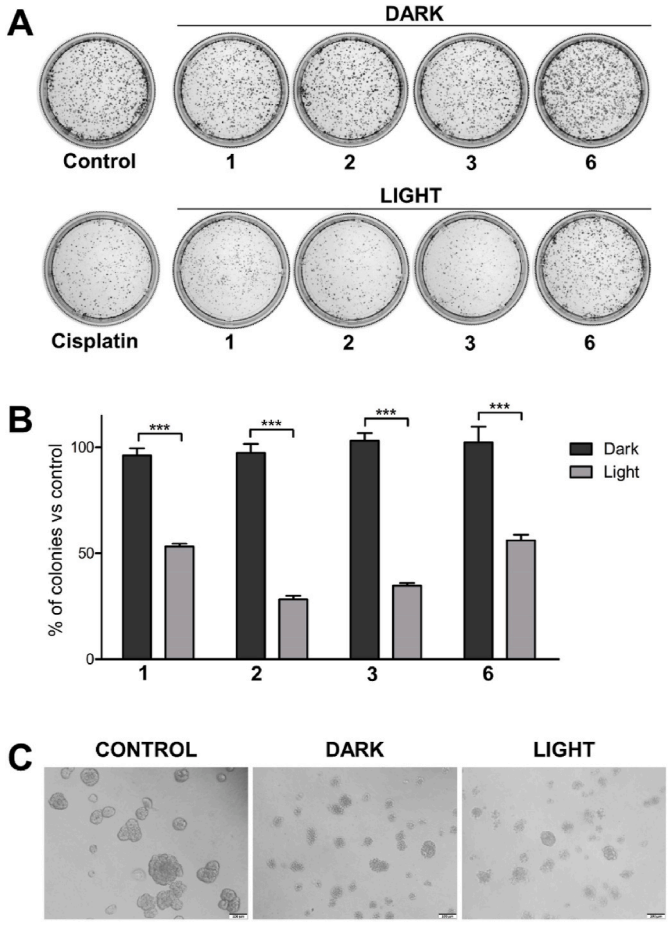

Fig. 8. Antitumoral activities A) Colony formation after exposure of PC-3 cells to complexes **1**, **2**, **3**, and **6** at the corresponding $IC_{50,light}$ in the dark or with blue-light irradiation (1 h, 460 nm, 24.1 J cm^{-2}). Control cells were incubated with the medium alone. Cisplatin at 5 μM was used as the positive control. B) Bar charts represent the percentage of colonies after each treatment relative to control cells (mean ± SD of 3 experiments. ***$p < 0.001$). C) Representative microscopy images of A549 spheroids treated with complex **1** at 20 μM in the dark or at 0.5 μM with blue-light irradiation. Untreated control A549 cells seeded on Geltrex™ formed rounded spheroids. Images show the growth-suppressing effect of the complex on spheroids in dark and light conditions after 48h of treatment. The scale bar represents 100 μm.

3.14. Intracellular ROS generation

The efficient generation of ROS within the cells is crucial for achieving successful outcomes in PDT. ROS are responsible for damaging different biomolecules, ultimately leading to cell death [70, 71]. The generation of intracellular ROS was analyzed using the carboxy-DCFDA probe, which is oxidized by various ROS within cells to the green fluorescent DCF product. Flow cytometry experiments showed that the fluorescence emission of the cells remained unaltered under dark conditions after the treatments with the complexes at their respective $IC_{50,light}$ (Fig. 9), indicating that ROS levels were not modified. However, upon irradiation, the fluorescence of the cells was significantly increased by complexes **1**, **2**, and **3**, with fold changes of 13.2 ± 0.9, 13.5 ± 2.6, and 9.6 ± 0.4, respectively. In the case of the Ru (III) complex **6**, fluorescence was increased by 6.2 ± 2.1-fold.

Finally, to ensure that the probe fluorescence accurately reflected the levels of ROS, the potential interference from the intrinsic fluorescence of the complexes was evaluated. To this end, HeLa cells were incubated with complexes **1**, **2**, **3** and **6** at their corresponding $IC_{50,light}$ and the cellular fluorescence was compared to that of untreated control cells by flow cytometry. The histograms corresponding to the different treatments showed no differences compared to control cells (Fig. S62), which confirmed that the fluorescence emission by the complexes is minimal at the $IC_{50,light.}$ Therefore, any disturbance of the complexes with these flow cytometry measurements could be excluded.

These findings collectively demonstrate the efficient generation of intracellular ROS by the photoactivated complexes, suggesting that their photocytotoxic activity is primarily attributed to their prooxidant properties.

3.15. Cellular internalization and localization

To ascertain whether the observed differences in the photocytotoxic

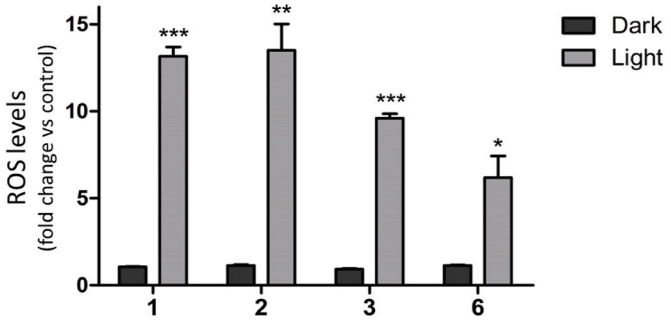

Fig. 9. Cellular ROS generation. HeLa cells were incubated with complexes **1**, **2**, **3**, and **6** at the corresponding $IC_{50,light}$ for 4 h and then maintained in the dark or exposed to blue-light irradiation for 1 h (460 nm, 24.1 J cm^{-2}). ROS levels were determined by flow cytometry using the carboxy-DCFDA probe. The mean ROS elevation ±SD relative to untreated control cells determined in three independent experiments are presented. *$p < 0.05$, **$p < 0.01$ and ***$p < 0.001$ versus control cells.

activity of the complexes, particularly between the Ir(III) complexes (**1**, **2**, and **3**) and the Ru(II) complex (**6**), were due to variations in their cellular internalization, HeLa cells were incubated with the complexes at 5 μM for 4 h and the intracellular metal content was quantified by ICP-MS. The results demonstrated a significantly lower level of internalization for the Ru(II) complex (**6**) compared to its Ir(III) counterpart (complex **3**) (0.7 ± 0.2 ng metal/10^6 cells vs 137.2 ± 31.7 ng metal/10^6 cells) (Fig. 10), which highlights the key influence of the metal on the capacity of the complexes to enter the cells. Similar high values were obtained for Ir(III) complex **1** (141.8 ± 16.5 ng metal/10^6 cells), while the Iridium content was lower in the case of complex **2** (56.2 ± 10.8 ng metal/10^6 cells). In general, the higher cellular accumulation of Ir(III) complexes correlated well with their enhanced photocytotoxic activity compared to the Ru(II) complex. Nevertheless, a direct correlation between Iridium content and the IC_{50} values of the complexes could not be established. Overall, these findings suggest that a minimum level of cellular uptake is essential for the photocytotoxic efficacy of these complexes.

Subsequently, the specific subcellular distribution of the compounds was examined, as it has a strong influence on their biological activity due to the short action radius of ROS once generated [72,73]. The studies were carried out by confocal microscopy with complex **1**, since it displays the highest quantum yield and fluorescence emission at physiological pHs. HeLa cells were chosen for the experiments, since they are morphologically spread, have a large cytoplasm, and are easy to transfect and express proteins, which makes them suitable for studying the entry and subcellular localization of the complex. Cells were incubated with complex **1** at 5 μM for 30–45 min and, after fixation with 4 % paraformaldehyde, permeabilized with 0.1 % Triton (TX-100) or 0.1 % saponin and stained with antibodies against early endosomal antigen 1 (EEA1) and lysobisphosphatidic acid (LBPA), which are early endosomes (EEs) and late endosomes/lysosomes (LEs/Lys) markers, respectively. Images acquired with a confocal microscope (Leica TCS SP5) indicated that the fluorescence of complex **1** was highly sensitive to fixation and Triton permeabilization and only faint staining was observed after saponin permeabilization. Notably, co-localization of complex **1** with few LBPA-positive endosomes (LEs/Lys) was detected, principally after 45 min of incubation (Fig. 11A). Interestingly, the diffuse pattern exhibited by complex **1** resembled that of the mitochondria. To mitigate the impact of fixation on the fluorescence emission of the complex, further characterization of its subcellular localization was analyzed *in vivo*. Co-localization studies were performed in HeLa cells expressing recombinant proteins specific to cell compartments (EEs, LEs/Lys, and mitochondria) fused with green (GFP), cherry, or dsRed fluorescent living colors. After a 30-min incubation with complex **1**, *in vivo* confocal images revealed a high degree of co-localization with dsRed-Mito (MitoRed) labeled mitochondria (Pearson's Correlation Coefficient, PCC = 0.723 ± 0.049). (Fig. 11B).

On the other hand, while co-localization of complex **1** with LEs/Lys markers CD63, Rab7, or Lamp2A was detected after 20—30 min of incubation by time-lapse video microscopy (Fig. 12A), no co-localization with Rab5 (EEs marker) was observed at any time (Fig. 12B). In line

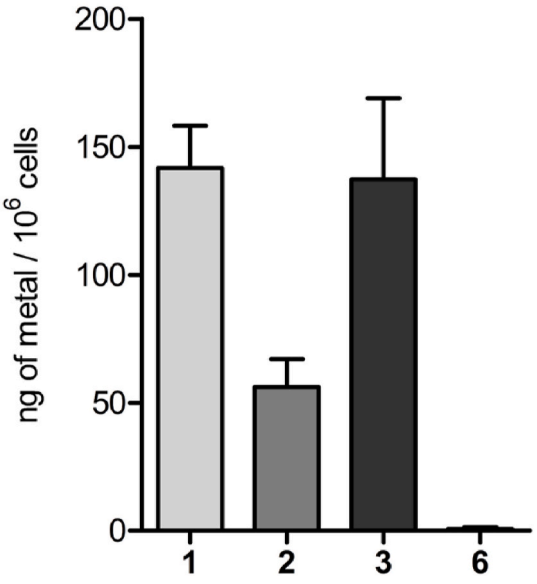

Fig. 10. Cellular internalization of complexes. HeLa cells were incubated with complexes **1**, **2**, **3**, and **6** at 5 μM. The amount of iridium or ruthenium per million cells after 4 h of treatment was determined by ICP-MS. Each bar in the graph represents the mean ± SD of three independent experiments.

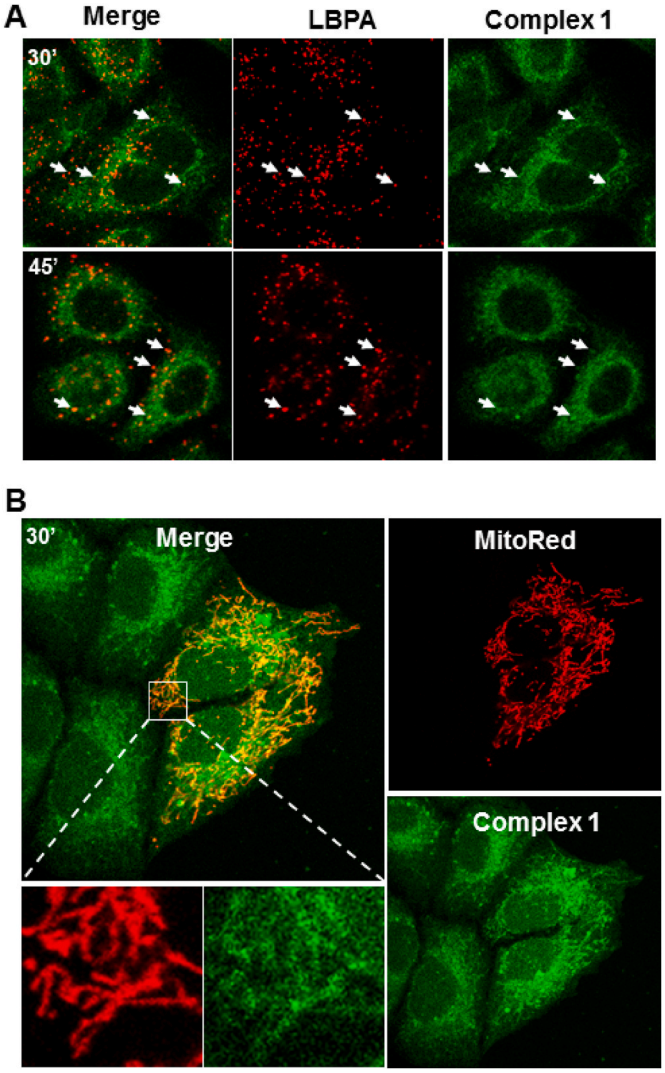

Fig. 11. Complex **1** localizes in lysosomes and mitochondria. A) HeLa cells were incubated with complex **1** (5 μM) at the indicated times and after fixation, LBPA was detected with a specific antibody and the secondary Alexa-555 anti-mouse. Images acquired with a confocal microscope (Leica TCS SP5) show some colocalization between LBPA (red channel) and the fluorescent complex **1** (green channel) (white arrows point selected colocalization staining). B) HeLa cells transiently expressing DsRed-Mito (MitoRed) were incubated with complex **1** (5 μM) during 30 min. In vivo images of complex **1** and MitoRed were sequentially acquired, using the inverted SP5-confocal microscope equipped with an incubation control system (37 °C, 5 % CO_2), with the 405 and 561 nm laser lines and the emission detection ranges 630–670 and 571–625 nm, respectively. Inset shows high magnification images of complex **1** localization in MitoRed-positive mitochondria.

with the previous cellular uptake data obtained by flow cytometry (Fig. 7), altogether suggest that complex **1** predominantly enters into cells by fast diffusion across the cell membrane and is then incorporated and retained in the acidic LEs/Lys without the need to follow the established endocytic internalization pathway.

In these microscopy experiments, rounded cells with blebbing (unhealthy cells) were detected at the end of the time-course experiment, as a result of the photoactivation of complex **1** by the irradiation at 405 nm. Given the cationic and lipophilic nature of the complex, its photodynamic activity could importantly affect mitochondria function and ultimately induce cell death. Therefore, the localization and delivery of complex **1** into mitochondria was analyzed in more detail using confocal video microscopy. GFP-Tom20 (Translocator Outer Membrane subunit) or MitoRed were ectopically transiently expressed in HeLa cells and

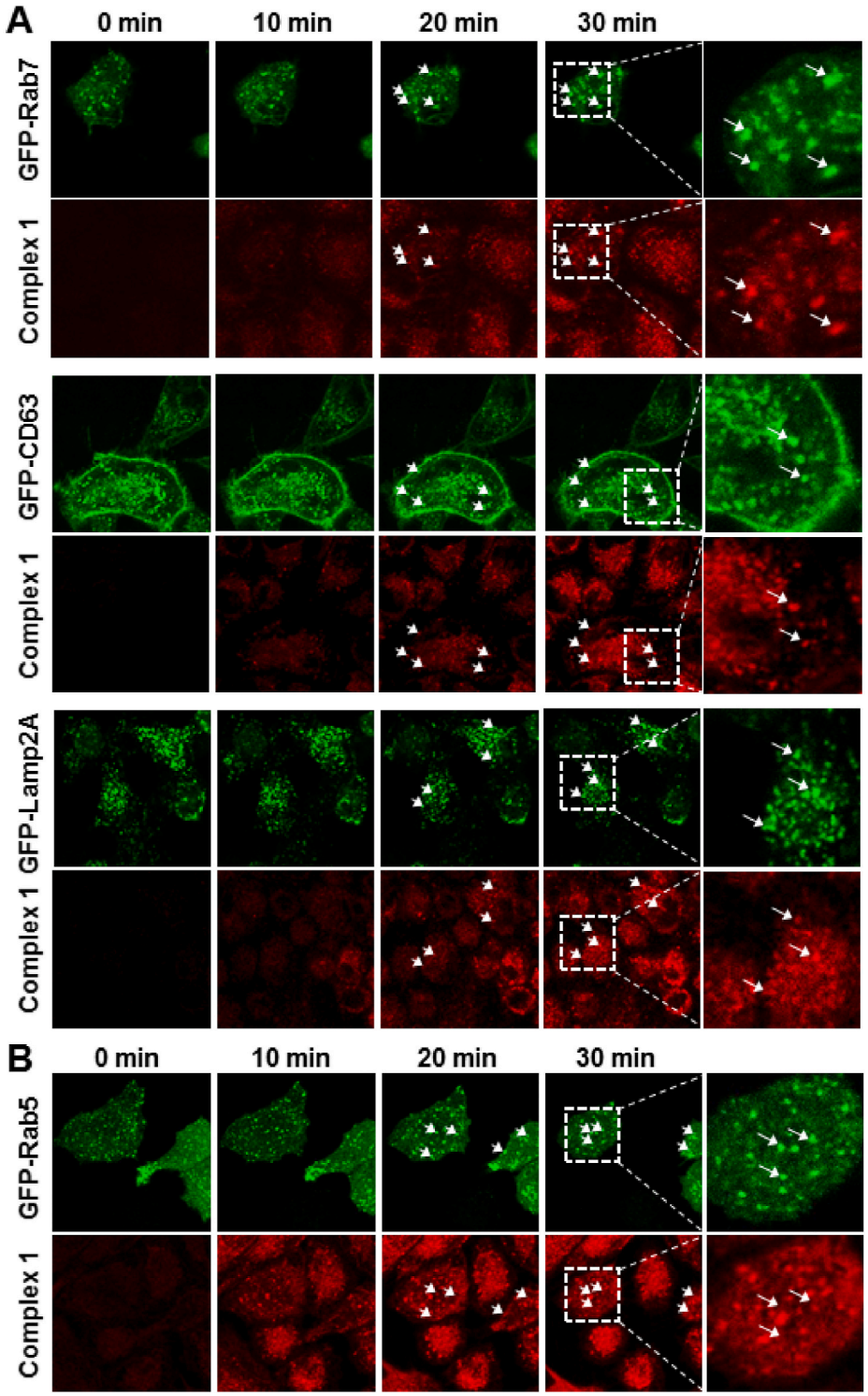

Fig. 12. HeLa cells expressing indicated recombinant GFP fusion proteins of the endolysosomal compartment (LEs/Lys) A) or Rab5 as a marker of early endosomes (EEs) B) were incubated at 37 °C with complex **1** (5 μM) and images acquired at the indicated times with *in vivo* SP5-confocal microscopy. After 20-30 min incubation time, colocalization among complex **1** (red channel) and the different markers of LEs/Lys (Rab7, CD63, and Lamp2A) but not Rab5 (green channel) was evident (white arrows).

complex **1** loading into mitochondria was visualized by confocal microscopy. Fig. 13A and B shows a fast incorporation of complex **1** in GFP-Tom20 and MitoRed labeled mitochondria, respectively (1 min or less). Importantly, after repeated irradiation to visualize the compound, the mitochondria began to lose their original morphology by progressively fragmenting and rounding.

It is to note that the acquired images revealed that the fluorescence of GFP-Tom20 was more sensitive to the phototoxicity generated by complex **1** (as it progressively loses fluorescence emission) than that of MitoRed (Fig. 13A and B). This could be explained by the different sensitivity of the fluorescent proteins to ROS generated by complex **1** or by the fact that GFP-Tom20 is closer to complex **1** than MitoRed. In fact, GFP-Tom20 is bound to the mitochondrial outer membrane and MitoRed is localized into the mitochondrial inner membrane and matrix. In addition, the fluorescence of complex **1** was also affected by the ROS generated by the compound (auto-bleaching). Fig. 13C shows in more detail that after 30 min incubation and irradiation of complex **1**, the compound decorated the edges, but not the MitoRed positive matrix of fragmented and rounded mitochondria. Complex **1** localization on mitochondria was further analyzed with MitoTracker Green, a selective fluorescent labelling dye of this organelle, which passively diffuses across the plasma membrane and then accumulates in active mitochondria in a potential-dependent manner. MitoTracker Green labels the mitochondrial matrix by reacting with free thiol groups of mitochondrial proteins [71,74]. HeLa cells pre-stained with MitoTracker Green were incubated with complex **1** and then irradiated (Fig. 13D). Complex **1** promptly labeled mitochondria and, after acquiring images, MitoTracker Green fluorescence rapidly disappeared. This result suggests that the phototoxicity generated by complex **1** affects mitochondrial membrane potential and functionality, which is in accordance with the proximity generation of ROS triggered by complex **1,** as described above (Fig. 9), in this organelle. In this line, fluorescence intensity of preloaded MitoTracker Green in HeLa cells was reduced after mitochondrial depolarization induced by carbonyl cyanide 3-chlorophenylhydrazone

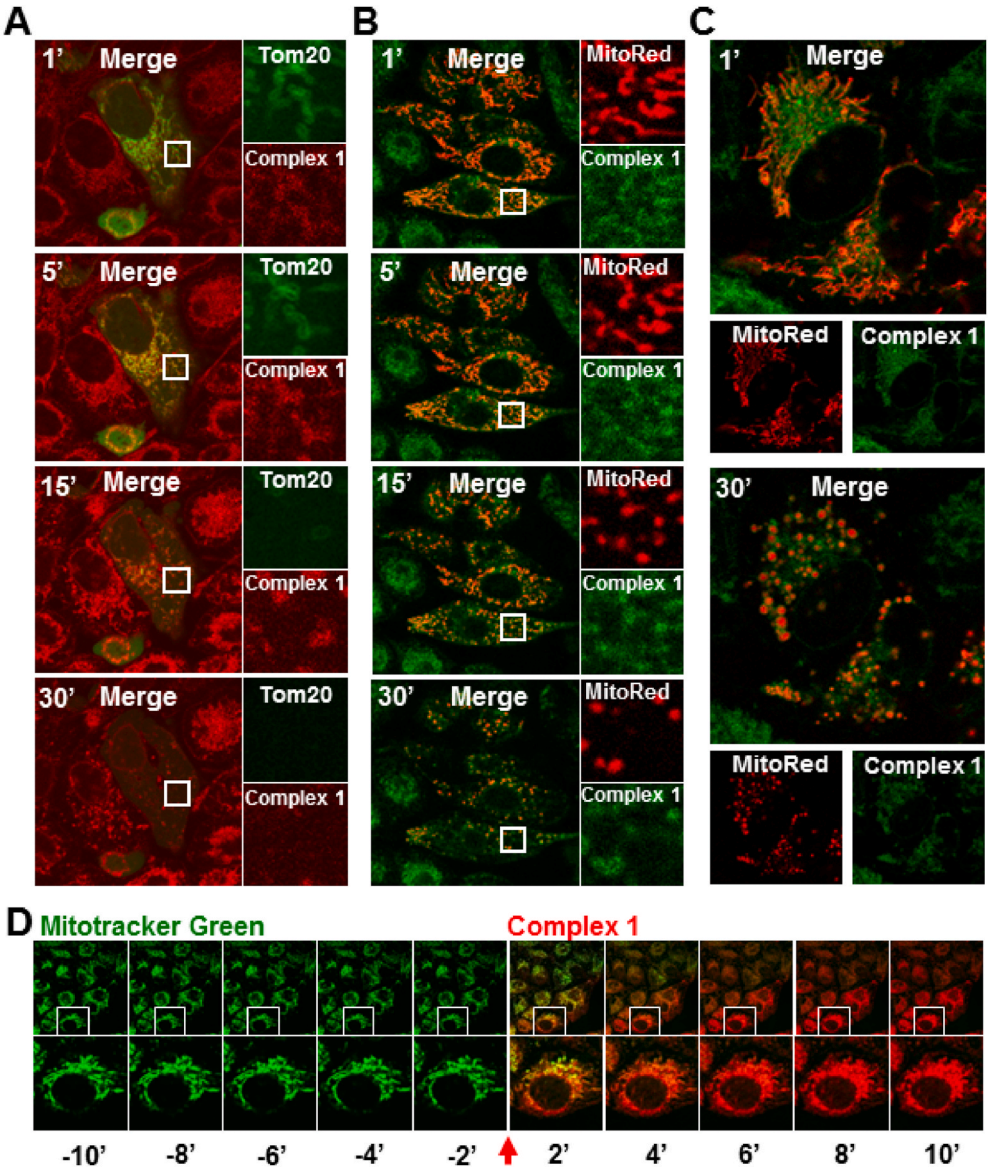

Fig. 13. Time-lapse video microscopy was performed in HeLa cells expressing GFP-Tom20 A) or MitoRed B, C) incubated with complex **1** (5 μM) during 30 min at 37 °C. Images were acquired at the indicated times with SP5-confocal microscopy and insets show high magnification areas to visualize complex **1** localization in labeled mitochondria. C) Images show the effect of complex **1** on mitochondrial morphology after 30 min of photoactivation. D) HeLa cells pre-stained with MitoTracker Green (30 min, 1 μM) were incubated with complex **1** (5 μM) and images acquired in a time-lapse confocal microscopy (TCS SP5-Leica). Images show that complex **1** rapidly incorporates into MitoTracker Green-labeled mitochondria and that after complex **1** irradiation MitoTracker Green quickly dissociates.

(CCCP) treatment [75]. In agreement with the cellular entry of the compound by diffusion and its rapid incorporation into mitochondria, independently of the endocytic pathway, the inhibition of dynamin using dynasore, which impaired transferrin internalization mediated by clathrin- and dynamin-dependent endocytosis, had no impact on the localization of complex 1 within GFP-Tom20 or MitoRed-labeled mitochondria (Fig. 14A). Consequently, dynasore also failed to alter the disruption of mitochondrial membrane potential induced by complex **1** (Fig. 14B).

Finally, double staining with markers of mitochondria, MitoRed or GFP-Tom20, and LEs/Lys compartments, GFP-Rab7 or Lysotracker-Red, was performed after 1 h of complex **1** incubation (Fig. 15A and B, respectively). Confocal microscopy images confirmed the accumulation of complex **1** in both mitochondria and LEs/Lys (PCC = 0.707 ± 0.058 and 0.762 ± 0.073, respectively).

3.16. Mitochondrial damage

After observing the rapid accumulation and effect of complex **1** in mitochondria, the impact of complexes **1**, **2**, **3**, and **6** on mitochondrial function was investigated. Mitochondrial membrane depolarization was analyzed as an indicator of mitochondrial damage, given its essential involvement in ATP synthesis and regulation of apoptosis [76]. Changes in membrane polarization were assessed by flow cytometry using the JC-1 fluorescent dye, which accumulates in healthy mitochondria in an MMP-dependent manner, undergoing a shift in its fluorescence emission from green to red. Red fluorescence emission was detected in 44.8 % of the control cells and similar fluorescence patterns were observed in cells treated with complexes **1**, **2**, **3**, and **6** at their respective $IC_{50,light}$ under dark conditions (Fig. 16 and Fig. S60). Notably, blue-light irradiation significantly reduced the population of red fluorescent cells by 32.7 %, 29.2 %, and 26.0 % for complexes **1**, **2**, and **3**, respectively, compared to the dark treatments. A similar effect was observed in cells exposed to the electronic chain uncoupler CCCP [77], demonstrating that the photodynamic activity of these complexes induces mitochondrial membrane depolarization. These results are consistent with the degeneration of the mitochondria observed by confocal microscopy (Fig. 14B). In contrast, Ru(II) complex **6** only reduced the red fluorescent population by 17.2 %, indicating a lower impact on mitochondrial functionality.

3.17. Lysosomal damage

Microscopy experiments also revealed the accumulation of complex **1** in LEs/Lys compartments (Fig. 12). Thus, the impact of the treatments on lysosomal integrity was evaluated using Acridine Orange (AO), which readily diffuses through cell and organelle membranes, binding with high affinity to nucleic acids. Due to its weak basic property, AO is protonated and sequestered in acidic environments such as lysosomes, shifting its green fluorescence emission towards red [78]. Microscopic images in Fig. 17 show that cells exposed to complexes **1**, **2**, **3**, and **6** at the $IC_{50,light}$ in the absence of light irradiation exhibited green fluorescent staining throughout the nucleus and cytoplasm along with cytosolic granular red fluorescence indicating intact lysosomes. After exposure to blue light, a similar pattern was observed in untreated control cells. However, cells exposed to the irradiated complexes showed a significant decrease in AO red fluorescence, indicating lysosomal damage. These findings are consistent with the lysosome-targeting activity described for other Ir(III) complexes bearing β-carboline ligands [60].

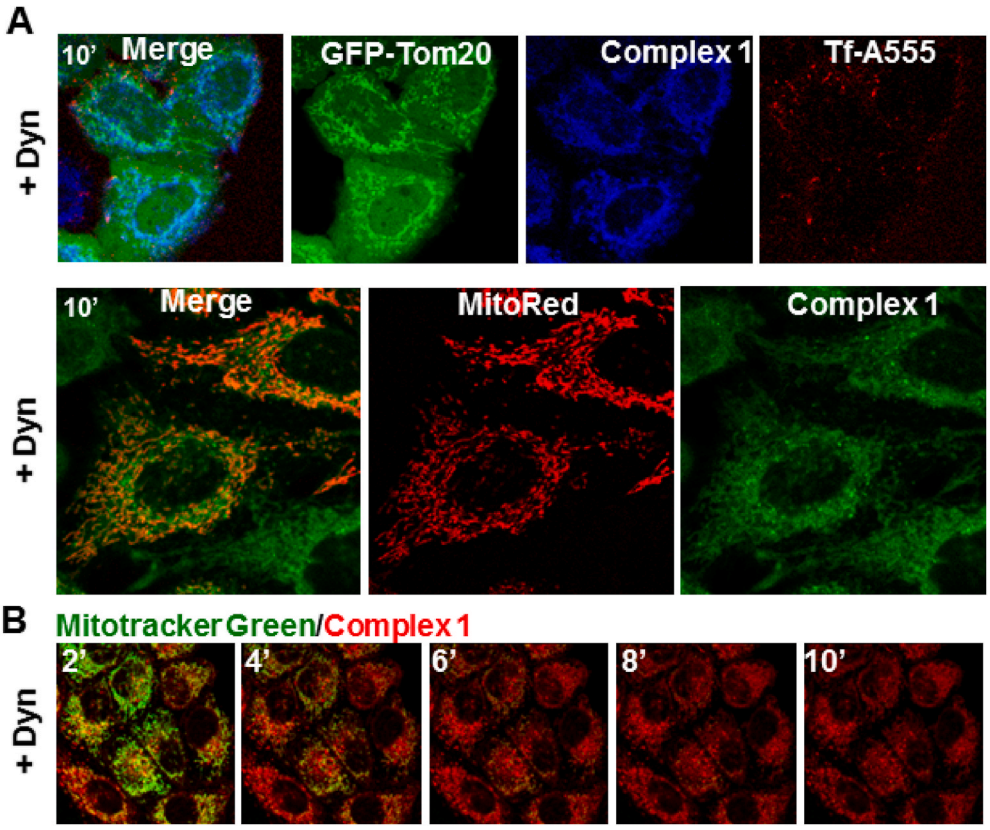

Fig. 14. A) HeLa cells transiently transfected with GFP-Tom20 (upper panels) or MitoRed (lower panels) were preincubated 20 min at 37 °C with dynasore (5 μM) and then further incubated 10 min with labeled transferrin (Tf-A555, 50 μg/mL; upper panels) and complex **1** (5 μM). *In vivo* SP5-confocal images, acquired with the corresponding settings, show effectiveness of the dynamin inhibitor dynasore avoiding transferrin endocytosis but not complex **1** association with GFP-Tom20 (upper panels) or MitoRed (lower panels) positives mitochondria. B) HeLa cells preincubated 30 min with dynasore (5 μM) and MitoTracker Green (1 μM) were further incubated with complex **1** (5 μM) at 37 °C for 10 min. Acquired images show MitoTracker Green fast dissociation from mitochondria after complex **1** photoactivation independently of dynamin activity.

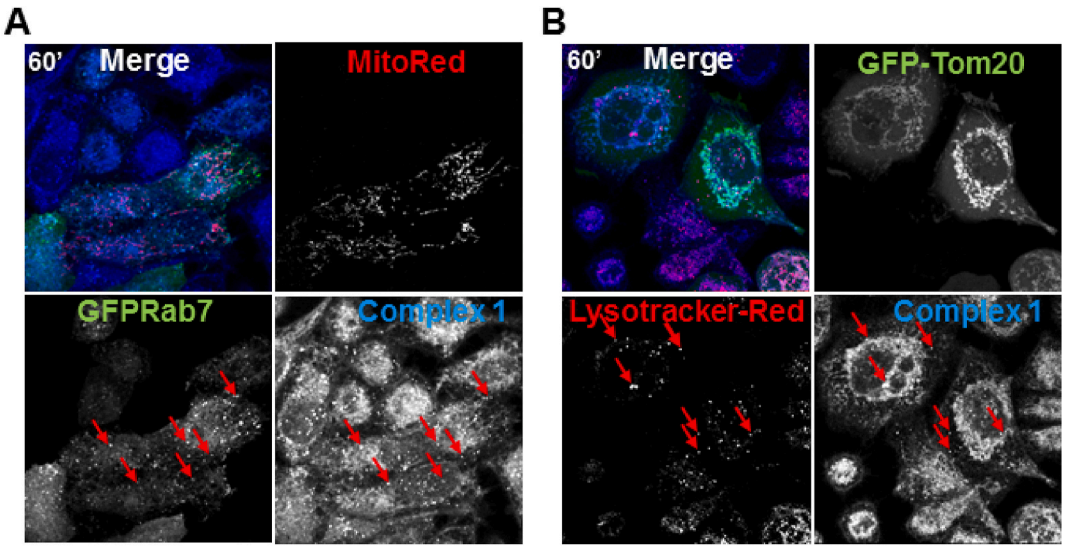

Fig. 15. HeLa cells expressing MitoRed and GFPRab7 (A) or GFP-Tom20 with Lysotracker-Red labeled-lysosomes (30 min, 100 nM) (B) were incubated 60 min with complex **1** and *in vivo* images acquired with the SP5-confocal microscope. Images show colocalization of complex **1** with GFPRab7 (A) or Lysotracker-Red (B) positive endolysosomes (red arrows) and MitoRed (A) or GFP-Tom20 (B) labeled mitochondria.

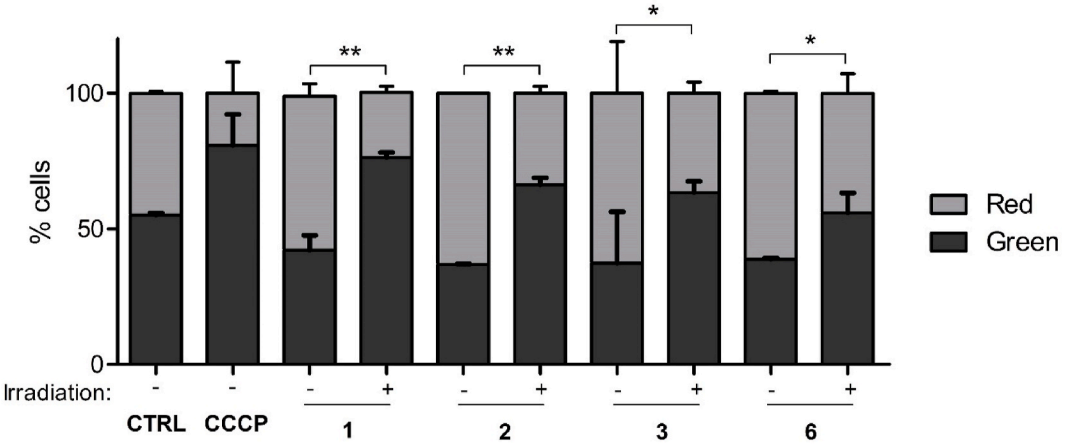

Fig. 16. Effect of the complexes on the mitochondrial membrane potential. HeLa cells were treated with complexes **1**, **2**, **3**, and **6** at the corresponding $IC_{50,light}$ in the dark or under light irradiation (1 h, 460 nm, 24.1 J cm^{-2}). The mitochondrial membrane uncoupler CCCP (5 μM) was used as a positive control. Cells incubated with medium alone were the negative control (CTRL). The percentage of cells showing JC-1 green and red fluorescence are represented (mean ± SD of three idependent experiments). Loss of MMP can be detected by the reduction of the percentage of cells showing red fluorescence. *p < 0.05 and **p < 0.01 vs control cells.

3.18. Cell death mechanism

The mechanism of action of the complexes was further elucidated by investigating the type of cell death induced upon their photoactivation. Disruption of both mitochondrial and lysosomal functions can initiate a programmed cell death through apoptosis [31,79]. Thus, cells were stained with annexin V-FITC, which enables the differentiation of apoptotic from necrotic cells, based on the presence of phosphatidylserine on the outer cell membrane of apoptotic cells (annexin +). Additionally, by measuring the permeability of the cell membrane to propidium iodide (PrI), it was possible to distinguish between early-stage apoptosis (PrI-) and late-stage apoptosis or necrosis (PrI+). A positive control for apoptosis was established using cisplatin (5 μM). Flow cytometry analysis of the cells after 24 h of treatment showed an increase in the percentage of cells in early apoptosis (annexin V+/PrI-) from 2.9 ± 0.3 % in control cells to 7.9 ± 6.9 %, 10.6 ± 9.0 %, and 12.2 ± 8.8 % in cells treated with photoactivated complexes **1**, **2**, and **3**, respectively (Fig. 18). A higher percentage of cells in late apoptosis (annexin +/PrI +) was detected, accounting for 23.5 ± 1.2 %, 65.1 ± 8.2 %, and 60.9 ± 2.9 % of the total cell population in cells treated with complexes **1**, **2**, and **3**, respectively, compared to 4.4 ± 0.1 % in control cells. However, the percentage of necrotic cells (annexin -/PrI +) was between 5 % and 10 % for all treatments. In the case of complex **6**, very few apoptotic or necrotic cells were detected at 24 h. However, at a longer incubation time (48 h) and higher concentration ($IC_{50,\ light}$ x 5), 12.3 ± 6.3 % of cells were found in early apoptosis and 16.9 ± 10.1 % in late apoptosis, while the percentage of necrotic cells remained unchanged (Fig. S61). These results are consistent with a reduced effect of complex **6** on MMP (Fig. 16), which would result in a reduced release of cytochrome *c* and other proteins involved in the activation of apoptosis [80]. Taken together, these results suggest that the photocytotoxic activity of the compounds primarily induces programmed cell death. Subsequently, ROS accumulation could cause massive oxidative damage to cellular structures, ultimately compromising cell membrane integrity and leading to late apoptosis or secondary necrosis [81]. Another interesting issue is about the excretion of complexes following phototherapy. Since the complexes have demonstrated the ability to induce apoptosis in target cells, excretion of the complexes is expected to be

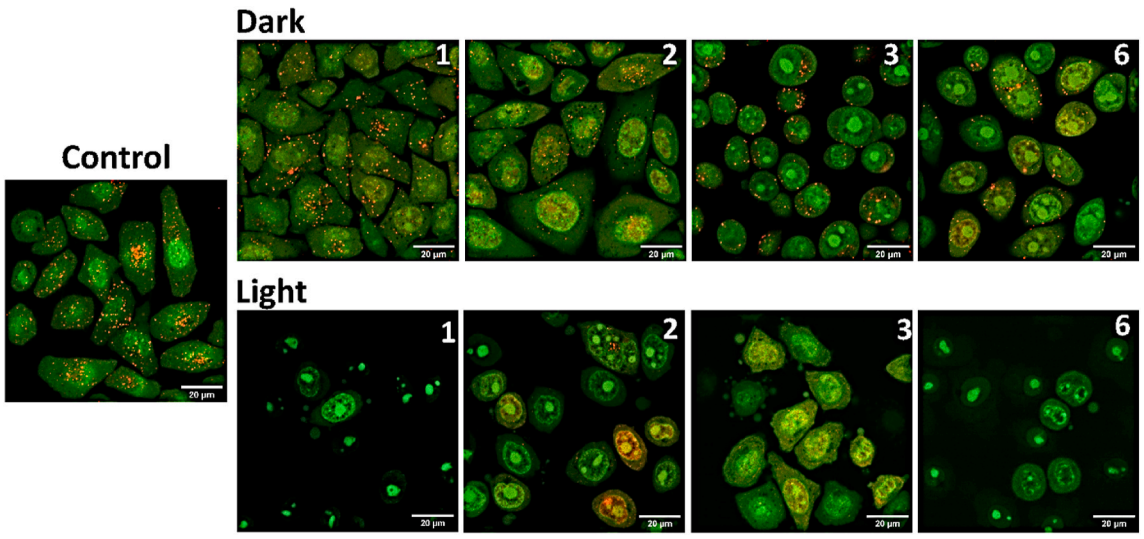

Fig. 17. Lysosomal damage. HeLa cells were treated with the complexes **1**, **2**, **3**, and **6** at the corresponding $IC_{50,light}$ in the dark or with light irradiation (1 h, 460 nm, 24.1 J cm^{-2}). Control cells were treated with medium alone under light conditions. Lysosomal damage was evaluated by confocal microscopy using AO staining (λ_{ex} = 488 nm). Cell cytoplasm and nucleoli were visualized in green (λ_{em} = 510 nm) while acidic cellular compartments, such as lysosomes, were visualized in red (λ_{em} = 625 nm). The scale bar represents 20 µm.

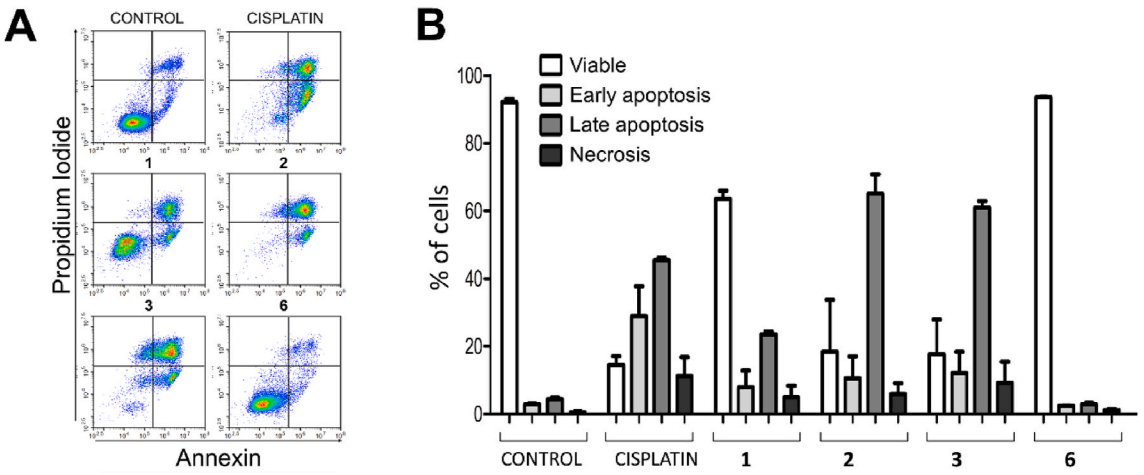

Fig. 18. Cell death mechanism. A) Representative flow cytometry histograms of HeLa cells treated with photoactivated complexes **1**, **2**, **3**, and **6** for 24 h at the corresponding $IC_{50,light}$ and double stained with propidium iodide and Annexin V-FITC. Cisplatin (5 µM) was used as positive control. B) Percentages of healthy, early apoptotic, late apoptotic, and necrotic cells (mean ± SD) after each treatment determined in two independent experiments.

facilitated by cellular processes mainly involving apoptotic pathways and subsequent clearance mechanisms in the organism.

3.19. Cell migration

Cell migration is an initial step in cancer metastasis. Mitochondria play an essential role in this process by providing the necessary energy supply for the modification of focal adhesions and remodeling of the cytoskeleton [17,18]. Considering the mitochondrial-targeted effects of the Ir(III) complexes, the impact of the treatments on the cell migration capacity was investigated using wound healing assays. In these assays, artificial wounds or "scratches" were created on confluent A549 cell monolayers, and cell movement was tracked using microscopy. As shown in Fig. 19, after the treatment in dark conditions, cell migration effectively allowed wound closure at 24 h (Fig. 19A), demonstrating a migration rate similar to that of the control cells (Fig. 19B). However, upon photoactivation, the wound healing percentage was significantly reduced, with the migration rate decreasing by 70—80 % in all cases compared to the control cells and cells treated in the dark. These findings suggested that the activity of the complexes could effectively inhibit the tumor cell migration.

4. Conclusions

We have prepared three series of Ir(III) (**1**–**3**) and Ru(II) (**4**–**9**) tris-chelate polypyridyl complexes and studied their photophysical and biological properties as potential PDT PSs. All the compounds are photostable and emissive in both acetonitrile and H_2O/DMSO (99:1) solutions. The N–H groups of these complexes are slightly acidic, which endows them with pH-responsive properties. The Ir(III) derivatives are more acidic than their Ru(II) analogues, ($5.9 < pK_a < 7.9$ for **1**–**3** vs $9.3 < pK_a < 10.3$ for **4**–**9**). Singularly, complex **3** exhibits a pK_a value of 5.9 and, as a result, it is deprotonated in most cell organelles at the respective physiological pH values. Indeed, the deprotonation at pH > 5.9 increases the electron density on the iridium center, which in turn causes a red-shift in its absorption profile and a dramatic emission quenching. Consistently, theoretical calculations performed for the deprotonated forms of the three Ir(III) complexes predict a large

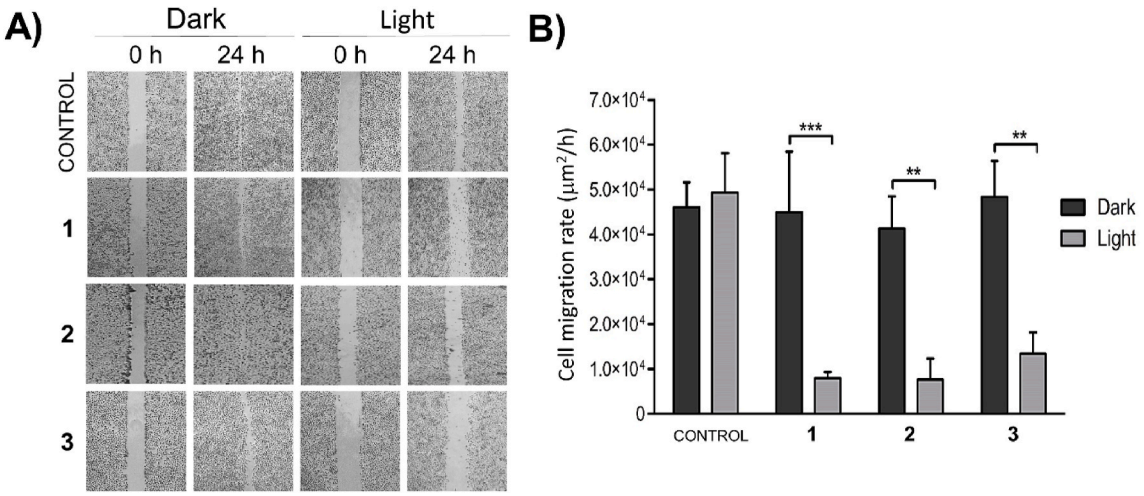

Fig. 19. Effect on cell migration. A) In vitro wound assay images showing the antimigratory effect of **1**, **2**, and **3** at the corresponding $IC_{50,light}$ on A549 cells 24 h after treatment. B) Cell migration rate (μm²/h) of cells exposed to the Ir(III) complexes under dark and light conditions. The bars represent the mean ± SD of three independent experiments. **p < 0.01 and ***p < 0.001 versus cells treated in the dark.

stabilization of ligand-centered states, resulting in T_1 (^{3}LC) states with longer lifetimes and higher $\Delta E_{T_1-^3MC}$ energy gaps compared to their protonated forms. This adjustment leads to less favorable radiative and non-radiative decays for the deprotonated forms of the Ir(III) derivatives and enhances their ability to generate ROS.

The Ir(III) complexes show high intrinsic cytotoxicity against different cancer cells, which increases significantly upon blue-light irradiation, reaching phototoxicity indices between 70 and 201 and $IC_{50,light}$ values in the low nanomolar range. Despite being less effective, green light irradiation could enhance the cytotoxic activity by 15–19 times for the Ir(III) complexes and 7.2 times for Ru(II) complexes compared to treatments in dark conditions. In the case of complex **3**, its activity is also significantly enhanced by red-light irradiation. Regarding the mechanism of action, extensive microscopy experiments with complex **1** have described that Ir(III) complexes can rapidly enter cells, independently of the endocytic pathway, and associate with the endo-lysosomal and mitochondrial cellular compartments. Photoactivation of the complexes triggers potent ROS generation and severely affects the mitochondrial and lysosomal functionality, ultimately leading to programmed cell death by apoptosis. In addition, Ir(III) complexes have been shown to effectively inhibit important cancer processes, including cell migration and colony formation. These results demonstrate the potential of these compounds for PDT of various types of cancer and their ability to inhibit processes associated with cancer malignancy, such as migration preceding metastasis or new tumor generation.

CRediT authorship contribution statement

Juan Sanz-Villafruela: Writing – original draft, Investigation. **Cristina Bermejo-Casadesus:** Methodology, Investigation, Formal analysis. **Elisenda Zafon:** Methodology, Investigation. **Marta Martínez-Alonso:** Investigation, Data curation. **Gema Durá:** Supervision. **Aranzazu Heras:** Supervision, Funding acquisition. **Iván Soriano-Díaz:** Data curation. **Angelo Giussani:** Methodology, Data curation. **Enrique Ortí:** Writing – original draft, Supervision, Funding acquisition, Conceptualization. **Francesc Tebar:** Writing – original draft, Methodology, Investigation. **Gustavo Espino:** Writing – original draft, Supervision, Methodology, Funding acquisition, Conceptualization. **Anna Massaguer:** Writing – original draft, Validation, Supervision, Methodology, Investigation, Funding acquisition.

Declaration of generative AI and AI-assisted technologies in the writing process

During the preparation of this work the authors used the DeepL and Grammarly tools in order to improve language and readability. The authors subsequently reviewed and edited the content as needed and take full responsibility for the content of the publication.

Declaration of competing interest

The authors declare that they have no known competing financial interests or personal relationships that could have appeared to influence the work reported in this paper.

Data availability

Data will be made available on request.

Acknowledgements

This work was supported by the Ministerio de Ciencia e Innovación/Agencia Estatal de Investigación of Spain (MCIN/AEI/10.13039/501100011033) (projects PID2021-127187OB-C21, PID2021-128569NB-I00, PID2020-115910RB-I00, PID2021-127187OB-C22, and CEX2019-000919-M). PhD students acknowledge their predoctoral grants to Universidad de Burgos (J.S.V., 2019/00002/008/001), University of Girona (C.B., IFUdG 2021), Generalitat de Catalunya (E.Z., AGAUR; 2021 FI_B 01036) and Generalitat Valenciana (I. S.D., CIACIF/2021/438), respectively. We thank M. Calvo, E. Coll and G. Martín and acknowledge the use of the Advanced Optical Microscopy Facility of the University of Barcelona (Spain).

Appendix A. Supplementary data

Supplementary data to this article can be found online at https://doi.org/10.1016/j.ejmech.2024.116618.

References

[1] A.M.P. Romani, Cisplatin in cancer treatment, Biochem. Pharmacol. 206 (2022) 115323, https://doi.org/10.1016/j.bcp.2022.115323.
[2] R. Oun, Y.E. Moussa, N.J. Wheate, The side effects of platinum-based chemotherapy drugs: a review for chemists, Dalton Trans. 47 (2018) 6645–6653, https://doi.org/10.1039/C8DT00838H.

[3] A.W. Lambert, D.R. Pattabiraman, R.A. Weinberg, Emerging biological principles of metastasis, Cell 168 (2017) 670–691, https://doi.org/10.1016/j.cell.2016.11.037.
[4] D. van Straten, V. Mashayekhi, H. de Bruijn, S. Oliveira, D. Robinson, Oncologic photodynamic therapy: basic principles, current clinical status and future directions, Cancers 9 (2017) 19, https://doi.org/10.3390/cancers9020019.
[5] D. Luo, K.A. Carter, D. Miranda, J.F. Lovell, Chemophototherapy: an emerging treatment option for solid tumors, Adv. Sci. 4 (2017) 1600106, https://doi.org/10.1002/advs.201600106.
[6] A.P. Castano, P. Mroz, M.R. Hamblin, Photodynamic therapy and anti-tumour immunity, Nat. Rev. Cancer 6 (2006) 535–545, https://doi.org/10.1038/nrc1894.
[7] M.K. Goshisht, N. Tripathi, G.K. Patra, M. Chaskar, Organelle-targeting ratiometric fluorescent probes: design principles, detection mechanisms, bio-applications, and challenges, Chem. Sci. 14 (2023) 5842–5871, https://doi.org/10.1039/D3SC01036H.
[8] B. Kar, U. Das, N. Roy, P. Paira, Recent advances on organelle specific Ru(II)/Ir (III)/Re(I) based complexes for photodynamic therapy, Coord. Chem. Rev. 474 (2023) 214860, https://doi.org/10.1016/j.ccr.2022.214860.
[9] J. Liu, C. Zhang, T.W. Rees, L. Ke, L. Ji, H. Chao, Harnessing ruthenium(II) as photodynamic agents: encouraging advances in cancer therapy, Coord. Chem. Rev. 363 (2018) 17–28, https://doi.org/10.1016/j.ccr.2018.03.002.
[10] E. Wachter, D.K. Heidary, B.S. Howerton, S. Parkin, E.C. Glazer, Light-activated ruthenium complexes photobind DNA and are cytotoxic in the photodynamic therapy window, Chem. Commun. 48 (2012) 9649, https://doi.org/10.1039/c2cc33359g.
[11] A. Zamora, G. Vigueras, V. Rodríguez, M.D. Santana, J. Ruiz, Cyclometalated iridium(III) luminescent complexes in therapy and phototherapy, Coord. Chem. Rev. 360 (2018) 34–76, https://doi.org/10.1016/j.ccr.2018.01.010.
[12] E. Zafon, I. Echevarría, S. Barrabés, B.R. Manzano, F.A. Jalón, A.M. Rodríguez, A. Massaguer, G. Espino, Photodynamic therapy with mitochondria-targeted biscyclometallated Ir(III) complexes. Multi-action mechanism and strong influence of the cyclometallating ligand, Dalton Trans. 51 (2022) 111–128, https://doi.org/10.1039/D1DT03080A.
[13] W.W. Qin, Z.Y. Pan, D.H. Cai, Y. Li, L. He, Cyclometalated iridium(III) complexes for mitochondria-Targeted combined chemo-photodynamic therapy, Dalton Trans. 49 (2020) 3562–3569, https://doi.org/10.1039/d0dt00180e.
[14] K. Qiu, Y. Liu, H. Huang, C. Liu, H. Zhu, Y. Chen, L. Ji, H. Chao, Biscylometalated iridium(III) complexes target mitochondria or lysosomes by regulating the lipophilicity of the main ligands, Dalton Trans. 45 (2016) 16144–16147, https://doi.org/10.1039/C6DT03328H.
[15] R. Horobin, F. Rashid-Doubell, J. Pediani, G. Milligan, Predicting small molecule fluorescent probe localization in living cells using QSAR modeling. 1. Overview and models for probes of structure, properties and function in single cells, Biotech. Histochem. 88 (2013) 440–460, https://doi.org/10.3109/10520295.2013.780634.
[16] M.D. Brand, A.L. Orr, I.V. Perevoshchikova, C.L. Quinlan, The role of mitochondrial function and cellular bioenergetics in ageing and disease, Br. J. Dermatol. 169 (2013) 1–8, https://doi.org/10.1111/bjd.12208.
[17] T.V. Denisenko, A.S. Gorbunova, B. Zhivotovsky, Mitochondrial involvement in migration, invasion and metastasis, Front. Cell Dev. Biol. 7 (2019), https://doi.org/10.3389/fcell.2019.00355.
[18] A.D. Scheid, T.C. Beadnell, D.R. Welch, Roles of mitochondria in the hallmarks of metastasis, Br. J. Cancer 124 (2021) 124–135, https://doi.org/10.1038/s41416-020-01125-8.
[19] S.E. Weinberg, N.S. Chandel, Targeting mitochondria metabolism for cancer therapy, Nat. Chem. Biol. 11 (2015) 9–15, https://doi.org/10.1038/nchembio.1712.
[20] P. Ghosh, C. Vidal, S. Dey, L. Zhang, Mitochondria targeting as an effective strategy for cancer therapy, Int. J. Mol. Sci. 21 (2020) 3363, https://doi.org/10.3390/ijms21093363.
[21] S. Fulda, L. Galluzzi, G. Kroemer, Targeting mitochondria for cancer therapy, Nat. Rev. Drug Discov. 9 (2010) 447–464, https://doi.org/10.1038/nrd3137.
[22] L. Groth-Pedersen, M. Jäättelä, Combating apoptosis and multidrug resistant cancers by targeting lysosomes, Cancer Lett. 332 (2013) 265–274, https://doi.org/10.1016/j.canlet.2010.05.021.
[23] T.M. Tsubone, W.K. Martins, C. Pavani, H.C. Junqueira, R. Itri, M.S. Baptista, Enhanced efficiency of cell death by lysosome-specific photodamage, Sci. Rep. 7 (2017) 6734, https://doi.org/10.1038/s41598-017-06788-7.
[24] J.A. Mindell, Lysosomal acidification mechanisms, Annu. Rev. Physiol. 74 (2012) 69–86, https://doi.org/10.1146/annurev-physiol-012110-142317.
[25] F. Geisslinger, M. Müller, A.M. Vollmar, K. Bartel, Targeting lysosomes in cancer as promising strategy to overcome chemoresistance—a mini review, Front. Oncol. 10 (2020), https://doi.org/10.3389/fonc.2020.01156.
[26] P. Yang, S. Zhang, K. Wang, H. Qi, Synthesis of pH-responsive cyclometalated iridium(III) complex and its application in the selective killing of cancerous cells, Dalton Trans. 50 (2021) 17338–17345, https://doi.org/10.1039/D1DT03042F.
[27] F.-X. Wang, M.-H. Chen, Y.-N. Lin, H. Zhang, C.-P. Tan, L.-N. Ji, Z.-W. Mao, Dual functions of cyclometalated iridium(III) complexes: anti-metastasis and lysosome-damaged photodynamic therapy, ACS Appl. Mater. Interfaces 9 (2017) 42471–42481, https://doi.org/10.1021/acsami.7b10258.
[28] W.K. Martins, N.F. Santos, C. de S. Rocha, I.O.L. Bacellar, T.M. Tsubone, A. C. Viotto, A.Y. Matsukuma, A.B. de P. Abrantes, P. Siani, L.G. Dias, M.S. Baptista, Parallel damage in mitochondria and lysosomes is an efficient way to photoinduce cell death, Autophagy 15 (2019) 259–279, https://doi.org/10.1080/15548627.2018.1515609.
[29] L. Xiong, Z. Liu, G. Ouyang, L. Lin, H. Huang, H. Kang, W. Chen, X. Miao, Y. Wen, Autophagy inhibition enhances photocytotoxicity of Photosan-II in human colorectal cancer cells, Oncotarget 8 (2017) 6419–6432, https://doi.org/10.18632/oncotarget.14117.
[30] W.K. Martins, R. Belotto, M.N. Silva, D. Grasso, M.D. Suriani, T.S. Lavor, R. Itri, M. S. Baptista, T.M. Tsubone, Autophagy regulation and photodynamic therapy: insights to improve outcomes of cancer treatment, Front. Oncol. 10 (2021), https://doi.org/10.3389/fonc.2020.610472.
[31] C. Pérez-Arnaiz, M.I. Acuña, N. Busto, I. Echevarría, M. Martínez-Alonso, G. Espino, B. García, F. Domínguez, Thiabendazole-based Rh(III) and Ir(III) biscyclometallated complexes with mitochondria-targeted anticancer activity and metal-sensitive photodynamic activity, Eur. J. Med. Chem. 157 (2018) 279–293, https://doi.org/10.1016/j.ejmech.2018.07.065.
[32] I. Echevarría, E. Zafon, S. Barrabés, M.Á. Martínez, S. Ramos-Gómez, N. Ortega, B. R. Manzano, F.A. Jalón, R. Quesada, G. Espino, A. Massaguer, Rational design of mitochondria targeted thiabendazole-based Ir(III) biscyclometalated complexes for a multimodal photodynamic therapy of cancer, J. Inorg. Biochem. 231 (2022) 111790, https://doi.org/10.1016/j.jinorgbio.2022.111790.
[33] J. Schindelin, I. Arganda-Carreras, E. Frise, V. Kaynig, M. Longair, T. Pietzsch, S. Preibisch, C. Rueden, S. Saalfeld, B. Schmid, J.-Y. Tinevez, D.J. White, V. Hartenstein, K. Eliceiri, P. Tomancak, A. Cardona, Fiji: an open-source platform for biological-image analysis, Nat. Methods 9 (2012) 676–682, https://doi.org/10.1038/nmeth.2019.
[34] C.A. Schneider, W.S. Rasband, K.W. Eliceiri, NIH Image to ImageJ: 25 years of image analysis, Nat. Methods 9 (2012) 671–675, https://doi.org/10.1038/nmeth.2089.
[35] C. Lee, W. Yang, R.G. Parr, Development of the Colle-Salvetti correlation-energy formula into a functional of the electron density, Phys. Rev. B 37 (1988) 785–789, https://doi.org/10.1103/PhysRevB.37.785.
[36] A.D. Becke, Density-functional thermochemistry. III. The role of exact exchange, J. Chem. Phys. 98 (1993) 5648–5652, https://doi.org/10.1063/1.464913.
[37] I. Soriano-Díaz, E. Ortí, A. Giussani, On the importance of equatorial metal-centered excited states in the photophysics of cyclometallated Ir(III) complexes, Dalton Trans. 52 (2023) 10437–10447, https://doi.org/10.1039/D3DT01404E.
[38] I. Soriano-Díaz, E. Ortí, A. Giussani, On the importance of ligand-centered excited states in the emission of cyclometalated Ir(III) complexes, Inorg. Chem. 60 (2021) 13222–13232, https://doi.org/10.1021/acs.inorgchem.1c01604.
[39] F. Weigend, R. Ahlrichs, Balanced basis sets of split valence, triple zeta valence and quadruple zeta valence quality for H to Rn: design and assessment of accuracy, Phys. Chem. Chem. Phys. 7 (2005) 3297, https://doi.org/10.1039/b508541a.
[40] F. Weigend, Accurate Coulomb-fitting basis sets for H to Rn, Phys. Chem. Chem. Phys. 8 (2006) 1057, https://doi.org/10.1039/b515623h.
[41] D.A. Pantazis, X.-Y. Chen, C.R. Landis, F. Neese, All-electron scalar relativistic basis sets for third-row transition metal atoms, J. Chem. Theor. Comput. 4 (2008) 908–919, https://doi.org/10.1021/ct800047t.
[42] R. Cammi, B. Mennucci, J. Tomasi, Fast evaluation of geometries and properties of excited molecules in solution: a tamm-dancoff model with application to 4-dimethylaminobenzonitrile, J. Phys. Chem. A 104 (2000) 5631–5637, https://doi.org/10.1021/jp000156l.
[43] F. Neese, Software update: the ORCA program system—version 5.0, WIREs Comput. Mol. Sci. 12 (2022) e1606, https://doi.org/10.1002/wcms.1606.
[44] F. Plasser, TheoDORE: a toolbox for a detailed and automated analysis of electronic excited state computations, J. Chem. Phys. 152 (2020), https://doi.org/10.1063/1.5143076.
[45] R.L. Martin, Natural transition orbitals, J. Chem. Phys. 118 (2003) 4775–4777, https://doi.org/10.1063/1.1558471.
[46] J.D. Rolfes, F. Neese, D.A. Pantazis, All-electron scalar relativistic basis sets for the elements Rb–Xe, J. Comput. Chem. 41 (2020) 1842–1849, https://doi.org/10.1002/jcc.26355.
[47] C. van Wüllen, Molecular density functional calculations in the regular relativistic approximation: method, application to coinage metal diatomics, hydrides, fluorides and chlorides, and comparison with first-order relativistic calculations, J. Chem. Phys. 109 (1998) 392–399, https://doi.org/10.1063/1.476576.
[48] J. Sanz-Villafruela, C. Martínez-Alonso, I. Echevarría, M. Vaquero, A. Carbayo, J. Fidalgo, A.M. Rodríguez, J.V. Cuevas-Vicario, J.C. Lima, A.J. Moro, B. R. Manzano, F.A. Jalón, G. Espino, One-pot photocatalytic transformation of indolines into 3-thiocyanate indoles with new Ir(III) photosensitizers bearing β-carbolines, Inorg. Chem. Front. 8 (2021) 1253–1270, https://doi.org/10.1039/D0QI01307B.
[49] S.M. Cloonan, R.B.P.P. Elmes, M. Erby, S.A. Bright, F.E. Poynton, D.E. Nolan, S. J. Quinn, T. Gunnlaugsson, D.C. Williams, Detailed biological profiling of a photoactivated and apoptosis inducing pdppz ruthenium(II) polypyridyl complex in cancer cells, J. Med. Chem. 58 (2015) 4494–4505, https://doi.org/10.1021/acs.jmedchem.5b00451.
[50] D. Havrylyuk, D.K. Heidary, L. Nease, S. Parkin, E.C. Glazer, Photochemical properties and structure-activity relationships of Ru II complexes with pyridylbenzazole ligands as promising anticancer agents, Eur. J. Inorg. Chem. 2017 (2017) 1687–1694, https://doi.org/10.1002/ejic.201601450.
[51] B.P. Sullivan, D.J. Salmon, T.J. Meyer, Mixed phosphine 2,2'-bipyridine complexes of ruthenium, Inorg. Chem. 17 (1978) 3334–3341, https://doi.org/10.1021/ic50190a006.
[52] A. Masschelein, L. Jacquet, A. Kirsch-De Mesmaeker, J. Nasielski, Ruthenium complexes with 1,4,5,8-tetraazaphenanthrene. Unusual photophysical behavior of the tris-homoleptic compound, Inorg. Chem. 29 (1990) 855–860, https://doi.org/10.1021/ic00329a056.
[53] R. Nasielski-Hinkens, M. Benedek-Vamos, Synthesis of Di- and tetra-substituted 1,4,5,8-tetra-azaphenanthrenes (pyrazino[2,3-f]quinoxalines), J. Chem. Soc. Perkin Trans. 1 (1975) 1229, https://doi.org/10.1039/p19750001229.

[54] I. Echevarría, M. Vaquero, R. Quesada, G. Espino, Synthesis of α-amino nitriles through one-pot selective Ru-photocatalyzed oxidative cyanation of amines, Inorg. Chem. Front. 7 (2020) 3092–3105, https://doi.org/10.1039/D0QI00580K.
[55] C. Tan, S. Lai, S. Wu, S. Hu, L. Zhou, Y. Chen, M. Wang, Y. Zhu, W. Lian, W. Peng, L. Ji, A. Xu, Nuclear permeable ruthenium(II) β-carboline complexes induce autophagy to antagonize mitochondrial-mediated apoptosis, J. Med. Chem. 53 (2010) 7613–7624, https://doi.org/10.1021/jm1009296.
[56] R. Gobetto, G. Caputo, C. Garino, S. Ghiani, C. Nervi, L. Salassa, E. Rosenberg, J.B. A. Ross, G. Viscardi, G. Martra, I. Miletto, M. Milanesio, Synthesis, electrochemical and electrogenerated chemiluminescence studies of ruthenium(II) bis(2,2′-bipyridyl){2-(4-methylpyridin-2-yl)benzo[d]-X-azole} complexes, Eur. J. Inorg. Chem. 2006 (2006) 2839–2849, https://doi.org/10.1002/ejic.200600099.
[57] S. Sreedharan, A. Sinopoli, P.J. Jarman, D. Robinson, C. Clemmet, P. A. Scattergood, C.R. Rice, C.G.W. Smythe, J.A. Thomas, P.I.P. Elliott, Mitochondria-localising DNA-binding biscyclometalated phenyltriazole iridium (III) dipyridophenazene complexes: syntheses and cellular imaging properties, Dalton Trans. 47 (2018) 4931–4940, https://doi.org/10.1039/C8DT00046H.
[58] A.F. Henwood, A.K. Pal, D.B. Cordes, A.M.Z. Slawin, T.W. Rees, C. Momblona, A. Babaei, A. Pertegás, E. Ortí, H.J. Bolink, E. Baranoff, E. Zysman-Colman, Blue-emitting cationic iridium(III) complexes featuring pyridylpyrimidine ligands and their use in sky-blue electroluminescent devices, J. Mater. Chem. C 5 (2017) 9638–9650, https://doi.org/10.1039/C7TC03110F.
[59] C. Momblona, C.D. Ertl, A. Pertegás, J.M. Junquera-Hernández, H.J. Bolink, E. C. Constable, M. Sessolo, E. Ortí, C.E. Housecroft, Exploring the effect of the cyclometallating ligand in 2-(pyridine-2-yl)benzo[d]thiazole-containing iridium (III) complexes for stable light-emitting electrochemical cells, J. Mater. Chem. C 6 (2018) 12679–12688, https://doi.org/10.1039/C8TC04727H.
[60] L. He, Y. Li, C.-P. Tan, R.-R. Ye, M.-H. Chen, J.-J. Cao, L.-N. Ji, Z.-W. Mao, Cyclometalated iridium(III) complexes as lysosome-targeted photodynamic anticancer and real-time tracking agents, Chem. Sci. 6 (2015) 5409–5418, https://doi.org/10.1039/C5SC01955A.
[61] L. He, C.-P. Tan, R.-R. Ye, Y.-Z. Zhao, Y.-H. Liu, Q. Zhao, L.-N. Ji, Z.-W. Mao, Theranostic iridium(III) complexes as one- and two-photon phosphorescent trackers to monitor autophagic lysosomes, Angew. Chem. Int. Ed. 53 (2014) 12137–12141, https://doi.org/10.1002/anie.201407468.
[62] P. Yang, S. Zhang, K. Wang, H. Qi, Synthesis of pH-responsive cyclometalated iridium(III) complex and its application in the selective killing of cancerous cells, Dalton Trans. 50 (2021) 17338–17345, https://doi.org/10.1039/D1DT03042F.
[63] Y. Cui, H.-J. Mo, J.-C. Chen, Y.-L. Niu, Y.-R. Zhong, K.-C. Zheng, B.-H. Ye, Anion-selective interaction and colorimeter by an optical metalloreceptor based on ruthenium(II) 2,2′-biimidazole: hydrogen bonding and proton transfer, Inorg. Chem. 46 (2007) 6427–6436, https://doi.org/10.1021/ic7004562.
[64] K.-C. Chang, S.-S. Sun, M.O. Odago, A.J. Lees, Anion recognition and sensing by transition-metal complexes with polarized NH recognition motifs, Coord. Chem. Rev. 284 (2015) 111–123, https://doi.org/10.1016/j.ccr.2014.09.009.
[65] C.A. Puckett, R.J. Ernst, J.K. Barton, Exploring the cellular accumulation of metal complexes, Dalton Trans. 39 (2010) 1159–1170, https://doi.org/10.1039/B922209J.
[66] M.M. Kim, A. Darafsheh, Light sources and dosimetry techniques for photodynamic therapy, Photochem. Photobiol. 96 (2020) 280–294, https://doi.org/10.1111/php.13219.
[67] B. Sun, J.N. Bte Rahmat, Y. Zhang, Advanced techniques for performing photodynamic therapy in deep-seated tissues, Biomaterials 291 (2022) 121875, https://doi.org/10.1016/j.biomaterials.2022.121875.
[68] N. Manduca, E. Maccafeo, R. De Maria, A. Sistigu, M. Musella, 3D cancer models: one step closer to in vitro human studies, Front. Immunol. 14 (2023), https://doi.org/10.3389/fimmu.2023.1175503.
[69] S. Sant, P.A. Johnston, The production of 3D tumor spheroids for cancer drug discovery, Drug Discov. Today Technol. 23 (2017) 27–36, https://doi.org/10.1016/j.ddtec.2017.03.002.
[70] I. Bacellar, T. Tsubone, C. Pavani, M. Baptista, Photodynamic efficiency: from molecular photochemistry to cell death, Int. J. Mol. Sci. 16 (2015) 20523–20559, https://doi.org/10.3390/ijms160920523.
[71] C. Imberti, P. Zhang, H. Huang, P.J. Sadler, New designs for phototherapeutic transition metal complexes, Angew. Chem. Int. Ed. 59 (2020) 61–73, https://doi.org/10.1002/anie.201905171.
[72] D. van Straten, V. Mashayekhi, H. de Bruijn, S. Oliveira, D. Robinson, Oncologic photodynamic therapy: basic principles, current clinical status and future directions, Cancers 9 (2017) 19, https://doi.org/10.3390/cancers9020019.
[73] A.P. Castano, T.N. Demidova, M.R. Hamblin, Mechanisms in photodynamic therapy: part one—photosensitizers, photochemistry and cellular localization, Photodiagnosis Photodyn. Ther. 1 (2004) 279–293, https://doi.org/10.1016/S1572-1000(05)00007-4.
[74] A.D. Presley, K.M. Fuller, E.A. Arriaga, MitoTracker Green labeling of mitochondrial proteins and their subsequent analysis by capillary electrophoresis with laser-induced fluorescence detection, J. Chromatogr. B 793 (2003) 141–150, https://doi.org/10.1016/S1570-0232(03)00371-4.
[75] B. Xiao, X. Deng, W. Zhou, E.-K. Tan, Flow cytometry-based assessment of mitophagy using MitoTracker, Front. Cell. Neurosci. 10 (2016), https://doi.org/10.3389/fncel.2016.00076.
[76] H. Vakifahmetoglu-Norberg, A.T. Ouchida, E. Norberg, The role of mitochondria in metabolism and cell death, Biochem. Biophys. Res. Commun. 482 (2017) 426–431, https://doi.org/10.1016/j.bbrc.2016.11.088.
[77] Y. Miyazono, S. Hirashima, N. Ishihara, J. Kusukawa, K. Nakamura, K. Ohta, Uncoupled mitochondria quickly shorten along their long axis to form indented spheroids, instead of rings, in a fission-independent manner, Sci. Rep. 8 (2018) 350, https://doi.org/10.1038/s41598-017-18582-6.
[78] X. Ge, S. Chen, X. Liu, Q. Wang, L. Gao, C. Zhao, L. Zhang, M. Shao, X.-A. Yuan, L. Tian, Z. Liu, Ferrocene-appended iridium(III) complexes: configuration regulation, anticancer application, and mechanism research, Inorg. Chem. 58 (2019) 14175–14184, https://doi.org/10.1021/acs.inorgchem.9b02227.
[79] D. Kessel, C.L. Evans, Promotion of proapoptotic signals by lysosomal photodamage: mechanistic aspects and influence of autophagy, Photochem. Photobiol. 92 (2016) 620–623, https://doi.org/10.1111/php.12592.
[80] N.L. Oleinick, R.L. Morris, I. Belichenko, The role of apoptosis in response to photodynamic therapy: what, where, why, and how, Photochem. Photobiol. Sci. 1 (2002) 1–21, https://doi.org/10.1039/b108586g.
[81] V. Nikoletopoulou, M. Markaki, K. Palikaras, N. Tavernarakis, Crosstalk between apoptosis, necrosis and autophagy, Biochim. Biophys. Acta Mol. Cell Res. 1833 (2013) 3448–3459, https://doi.org/10.1016/j.bbamcr.2013.06.001.